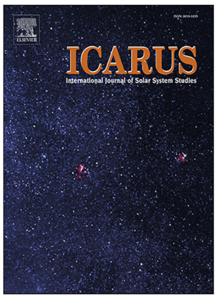

Vertical distribution of water vapour for Martian northern hemisphere summer in Mars year 28 from Mars Climate Sounder

R. Lolachi, P.G.J. Irwin, N.A. Teanby

PII: S0019-1035(22)00245-7
DOI: https://doi.org/10.1016/j.icarus.2022.115141
Reference: YICAR 115141

To appear in: *Icarus*

Received date : 4 June 2021
Revised date : 8 June 2022
Accepted date : 15 June 2022

Please cite this article as: R. Lolachi, P.G.J. Irwin and N.A. Teanby, Vertical distribution of water vapour for Martian northern hemisphere summer in Mars year 28 from Mars Climate Sounder. *Icarus* (2022), doi: https://doi.org/10.1016/j.icarus.2022.115141.

Vertical Distribution of Water Vapour for Martian Northern Hemisphere Summer in Mars Year 28 from Mars Climate Sounder

R. Lolachi[a,b,c,d,*], P.G.J. Irwin[d], N.A. Teanby[e]

[a]*Center for Space Sciences and Technology, University of Maryland, Baltimore County, Baltimore, MD 21250, USA*
[b]*NASA Goddard Space Flight Center, Greenbelt, MD 20771, USA*
[c]*Center for Research and Exploration in Space Science and Technology, NASA/GSFC, Greenbelt, MD 20771, USA*
[d]*Atmospheric, Oceanic & Planetary Physics, Department of Physics, University of Oxford, Clarendon Laboratory, Parks Road, Oxford, OX1 3PU, UK*
[e]*School of Earth Sciences, University of Bristol, Wills Memorial Building, Queens Road, Bristol, BS8 1RJ, UK*

Abstract

We present, for the first time, retrievals of the vertical distribution of water vapour from Mars Climate Sounder (MCS) aboard Mars Reconnaissance Orbiter (MRO), an original goal of the mission compromised by channel filter performance issues. To work around this problem a two-stage retrieval has been developed and was applied to MCS observations for MY28 NH summer (L_s=111–173°, 26 September 2006 to 27 January 2007). Retrievals were consistent with observations by other instruments for both column abundances (e.g., peak NH summer column abundance of 70 pr. µm compared with 50 pr. µm in the literature) and vertical profiles. Other key results are nightside vertical profiles of water vapour (retrieved for the first time) and interaction of atmospheric water vapour with the aphelion cloud belt. Seasonal changes in the hygropause (a proxy for condensation level) are reflected in changes in the cloud belt. During late northern summer, when the hygropause level is high at the equator and tropics, the cloudbase is higher (increasing by ≈10 km from 25 to 35 km) and the belt is weaker.

Keywords: MCS, Mars, Mars atmosphere, profile retrieval, water vapour

---

[*] Corresponding author
Email address: rlolachi@umbc.edu (R. Lolachi)

---

1. Introduction

Water vapour is a very active and dynamic trace gas in the atmosphere of Mars. Studying it helps us to understand the sources and sinks of water on Mars such as the reservoirs at the poles (Montmessin et al., 2017b) and the permafrost at the mid and high latitudes (Boynton et al., 2002). It can tell us about the evolution of water and the atmosphere on Mars, including the posited ancient ocean (Baker et al., 1991; Read and Lewis, 2004) and ultimately about the habitability past or present on the red planet. To understand its behaviour more fully in the atmosphere it is important to understand its vertical distribution. Though water vapour has been known to be present in the atmosphere for some time (Spinrad et al., 1963), it is has only been relatively recently that sustained direct observation of its vertical distribution has become possible. At an indirect level this can be done by examining the condensation levels (derived from temperature profiles) for water vapour along with their seasonal variation. This variation can be seen in results from Mars Global Surveyor's Thermal Emission Spectrometer (TES) (Smith, 2002), and Mars Express' Visible and Infrared Mineralogical Mapping Spectrometer (OMEGA) (Maltagliati et al., 2011b) and Ultraviolet and Infrared Atmospheric Spectrometer (SPICAM) (Montmessin et al., 2017a).

The condensation levels are driven by atmospheric temperature. At the local/regional level normal factors such as latitude, time of day, and season affect temperature and concomitantly condensation levels. In addition, superimposed on this local/regional variation, global atmospheric temperatures and condensation levels are affected by the planet's solar distance. Observing the zonally averaged condensation level, it is seen that when the planet is nearer aphelion (currently at areocentric longitude L_s=70°) between L_s=0° and 180° the atmosphere is relatively cool and so the condensation level is low (around 10–20 km), as the planet nears perihelion (currently at L_s=251°) the atmospheric temperature rises and so accordingly does the condensation level to over 40 km (Smith, 2002). This rising and falling of the average condensation level has an effect on water vapour transport around the planet. During the warmer perihelion season, when the condensation level is high, water vapour can be transported from south to north via the Hadley circulation without condensing. Near aphelion the condensation level is lower and water vapour cannot be transported via the Hadley circulation without condensing leading to the creation of the water ice aphelion cloud belt (Smith, 2002; Montmessin et al., 2017b; Sefton-Nash et al., 2013). This could explain the relative maximum in water vapour column abundances observed at low northerly latitudes during the autumn (L_s=180–270°) and winter (L_s=270–360°), and the much larger latitudinal gradient in water vapour in the northern summer (L_s=90–180°) as compared to the southern summer (L_s=270–360°) (Clancy et al., 1996; Smith, 2002).

The earliest direct measurements of water vapour vertical structure were made by Rodin et al. (1997) and Krasnopolsky et al. (1991) using the Phobos/Auguste experiment. Their profile showed very dry atmospheric conditions above ~30 km with the volume mixing ratio dropping down as low as 3 ± 2 ppm. At 20–30 km (at the condensation level) the mixing ratio showed a steep rise with decreasing altitude (attributed to cloud formation here by Rodin et al. 1997) over a scale height of 2.5 km to a fairly constant mixing ratio down to the bottom of the observed altitude range at 10 km.

Newer results have since been obtained using data from the Ultraviolet and Infrared Atmospheric Spectrometer (SPICAM) on Mars Express (Fedorova et al., 2009; Maltagliati et al., 2011a, 2013; Fedorova et al., 2018), the Compact Reconnaissance Imaging Spectrometer for Mars (CRISM) on Mars Reconnaissance Orbiter (MRO) (Clancy et al., 2017), and the ExoMars Trace Gas Orbiter (TGO) with the Atmospheric Chemistry Suite (ACS) and Nadir Occultation for Mars Discovery spectrometer suite (NOMAD) instruments aboard (Vandaele et al., 2019).

Until recently it was assumed that water vapour always had the simple vertical structure seen in Phobos/Auguste results—a constant volume mixing ratio (VMR) up to the condensation level with rapid drop-off above, but the newer results have shown this not to be the case. In agreement with the older results, the newer observations of seasonal change have shown that during the late northern spring and early summer the vertical extent of water vapour is mainly limited to lower altitudes in line with the low condensation levels at this time of year (Fedorova et al., 2009; Maltagliati et al., 2011a, 2013; Clancy et al., 2017; Fedorova et al., 2018; Vandaele et al., 2019). As the season progresses into southern spring and summer, and the condensation levels rise, the water vapour altitude range increases as well (Maltagliati et al., 2013). The more surprising finds from these vertical profile measures have been the observation of extensive supersaturation (Maltagliati et al., 2011a), detached layers of water (Maltagliati et al., 2013), transport to higher altitudes and a variable correlation with dust aerosol related to dust storm activity (Fedorova et al., 2018; Vandaele et al., 2019), and at times highly variable vertical profiles changing on the order of days (Maltagliati et al., 2013).

With this rich variety of instruments at Mars extensive observation of the seasonal evolution of vertical water vapour profile has become possible. It was hoped that Mars Climate Sounder (MCS) would have been the first instrument after Phobos/Auguste to make extensive continuous measurements of water vapour vertical distribution, but this was hampered by problems with bandpass-broadening in the water vapour and dust channels. In this paper we develop a new approach for measuring water vapour profiles from the MCS data and use this to investigate novel aspects of Mars' water cycle.

2. Instrument, Challenges & Observations

2.1. Mars Climate Sounder

Mars Climate Sounder (MCS) is an infrared radiometer aboard NASA's Mars Reconnaissance Orbiter (MRO) with the purpose of observing the spatial and temporal variation of the atmosphere, with regard to the vertical and horizontal distributions of temperature, pressure, dust and water vapour (McCleese et al., 2007). MRO is presently in a near-polar (92.6° inclination), near circular, low altitude (~300 km), 03h/15h sun-synchronous orbit. The spacecraft passes over any given point of the planet's surface at the same local mean solar time on the dayside and has a local mean solar time 12 hours later when passing over the nightside, except for near the poles. MCS has nine spectral channels ranging from 0.3–50 μm that can observe in limb and on-planet (nadir and off-nadir) viewing geometries for both in and off-track (sideways-looking) observations. Each channel consists of a 21-element linear thermopile detector array, with each detector mapping a 5 km × 8.5 km field of view (FOV) when used in the limb viewing geometry (covering a range of 105 km) and a 1 km × 1.7 km FOV for a nadir geometry. The vertical resolution of 5 km corresponds to approximately half an atmospheric scale height.

The instrument's nine spectral channels are split into two groups with corresponding focal planes and telescopes. The first group are the six 'A' channels, where channels A1–A5 use mid-infrared optical interference filters (400–870 cm^{-1}) with A6 being a broadband channel in the visible. The second group are the three 'B' channels, using far infrared mesh filters (220–340 cm^{-1}). More details on the spectral characteristics of each channel can be found in McCleese et al. (2007) and Kleinböhl et al. (2009). MCS started taking data in September 2006, corresponding to $L_s \approx 110°$ in Mars Year 28 (MY28) under the system established by Clancy et al. (2000).

In a nominal cycle, a sequence of eight two-second in-track limb observations are acquired preceded by an on-planet observation and followed by a space view (Kleinböhl et al., 2009; McCleese et al., 2007). In order to increase the signal-to-noise ratio, an average is taken of the neighbouring limb observations. However, the first three of these limb measurements contain thermal transients from the preceding, warmer, on-planet observations. Consequently, the last five measurements in the sequence of eight are used for the average. Finally, the limb observations are paired with the nearest on-planet observation within a 1° great-circle distance. At the beginning of the mission, the on-planet observations were mostly nadir views. However, after MCS suffered an elevation slew impediment this was changed to off-nadir views to reduce the risk of MCS getting stuck (Kleinböhl et al., 2009).

2.2. Water Vapour Channel Broadening

The B2/B3 channel pair were designed to enable retrieval of water mixing ratio independently of dust. The channels were spectrally co-located, with the wide B2 (220–260 cm^{-1}), and the narrow B3 (230–245 cm^{-1}), sitting within the B2 bandpass. The B2 channel included two strong water absorption bands while the narrow B3 channel was positioned between the water bands. With common central wavelengths, they should have had similar sensitivity to dust but significantly different sensitivities to water vapour. This should have allowed simultaneous retrieval of water vapour and dust, given separate information about the temperature profile. However, the channels failed

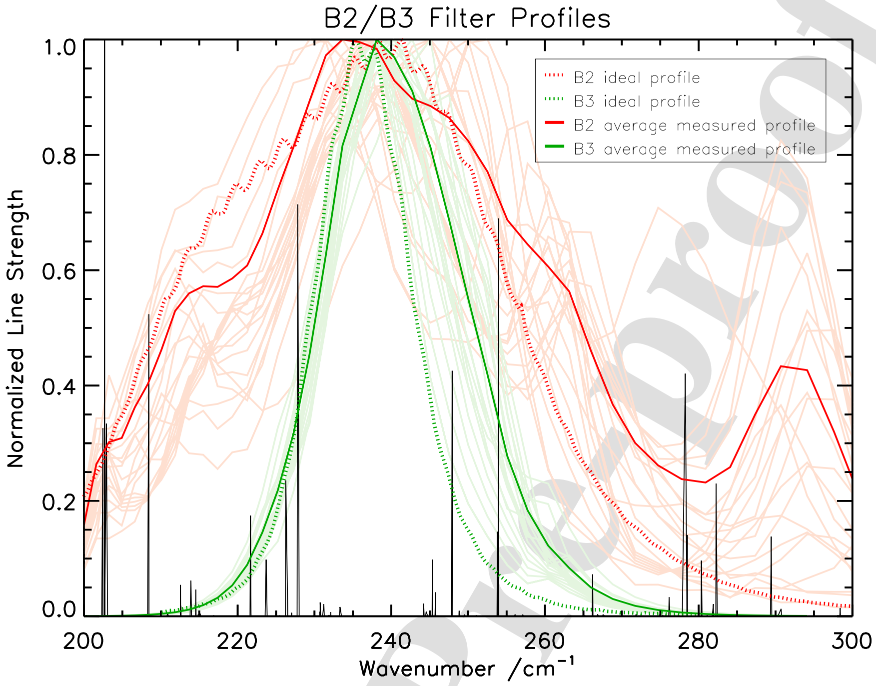

Figure 1: Comparison between the designed (dotted line) and measured (solid line) detector-averaged filter response profiles for B2 (red) and B3 (green) with water line strengths (black lines). Profiles and water lines have all been normalized. Also shown in pale red and green are the measured response profiles for individual detectors. Dust extinction is not shown, but is approximately constant over the full spectral interval. Broadening in B3 can be easily seen along with the smaller broadening effect in B2, which also features an additional peak. This broadening stops the pair from being used to retrieve water vapour independently of dust as originally conceived; an alternative methodology is needed.

to meet their design specification with bandpasses much wider than originally planned, as revealed in tests just prior to launch (McCleese et al., 2007). These showed severe broadening in B3 and a similar, though smaller, effect in B2 (see Fig. 1). Additionally, different filter responses are seen for each detector. Consequently, simultaneous retrievals of water vapour and dust are no longer possible, shown by sensitivity studies discussed in Section 4. Instead, a two-stage retrieval approach, using only B2 must be implemented. This is discussed in Section 5. Further details of the broadening and results of laboratory analyses into the problem are given in Lolachi (2019).

2.3. Observations

MCS data used comes from the observations starting with the beginning of the mission on 24 September 2006 (L_s=111°) and extending to the 27 January 2007 (L_s=173°), during northern hemisphere (NH) summer MY28 on Mars. These data were taken before MCS suffered an elevation slew impairment (see Kleinböhl et al., 2009, for details) and hence includes fully calibrated nadir and limb data. The observations have been split into two seasonal blocks, L_s=111–140° and L_s=140–173°. These will be referred to as 'early NH summer' and 'late NH summer'. This was done to allow easy comparison with binned CRISM data and also to observe seasonal variation. These seasonal blocks were further divided into dayside (09–21h LST) and nightside (21h–09h LST) observations.

3. Radiative Transfer

3.1. Software

This study was conducted using Oxford's planetary radiative transfer and retrieval software suite, NEMESIS (Non-linear optimal Estimator for Multivariate spectral analysis) (Irwin et al., 2008). Within the suite is a MCS-specific version, NemesisMCS. Hereafter, any references to NEMESIS are with regards to NemesisMCS. NemesisMCS includes a procedure for integrating the measured FOVs of the detectors which is discussed in Section 3.2. For radiative transfer, the software makes use of either a line-by-line or correlated-k method (Lacis and Oinas, 1991). For this analysis, the correlated-k method is employed, due to its computational expediency, with k-distribution tables constructed for carbon dioxide and water vapour, the main spectroscopically active atmospheric gases in the MCS wavelength range. For non-scattering (thermal emission) simulations NEMESIS does not use the plane-parallel approximation. Instead, it assumes a spherical atmosphere for both limb and nadir calculations. In the multiple scattering case, the radiance is calculated in a plane-parallel atmosphere at a given point, but the forward model integrates the radiative transfer equation along the limb/nadir path in a curved atmosphere. This study assumes a non-scattering atmosphere.

The retrieval algorithm employed by the code is an optimal estimation method (Rodgers, 2000). It starts with a first-guess, or *a priori* profile and seeks to reduce the difference between the measured and modelled radiances via minimisation of the cost function (Irwin et al., 2008)

$$\phi = (\mathbf{y_m} - \mathbf{y_n})^{\mathrm{T}} \mathbf{S}_{\epsilon}{}^{-1} (\mathbf{y_m} - \mathbf{y_n}) + (\mathbf{x_n} - \mathbf{x_a})^{\mathrm{T}} \mathbf{S_a}{}^{-1} (\mathbf{x_n} - \mathbf{x_a}) \,, \tag{1}$$

where $\mathbf{y_m}$ are the measured radiances, $\mathbf{y_n}$ are the modelled radiances for the trial atmosphere represented by model state vector $\mathbf{x_n}$, $\mathbf{S}_{\epsilon}$ is the measurement covariance matrix (containing measurement error and the estimated forward modelling error), $\mathbf{x_a}$ is *a priori* state vector and $\mathbf{S_a}$ is the *a priori* covariance matrix.

From Eq. 1, it can be seen that additional constraint is applied to the solution via the second term related to the *a priori*. The *a priori* provides additional information to the retrieval and also provides smoothing which helps remove unrealistic oscillations introduced by over-fitting to the noise. For the covariance matrix, $\mathbf{S_a}$, diagonal elements are set to the square of the estimated *a priori* errors and off-diagonal elements represent cross-correlation (Irwin et al., 2008; Rodgers, 2000).

For more information on the software see Irwin et al. (2008). NEMESIS was used for all radiative transfer modelling and retrieval calculations in this study.

3.2. Field of View Rotation/Averaging and B2 Filter Bandpasses

Despite all the efforts taken to ensure FOV functions with low wings, the instrument as flown has been observed with FOV functions that have large wings. This effect was observed when the top detectors looking at space during limb observations were not registering zero radiance (Hurley et al., 2014; Kleinböhl et al., 2009). These large wings mean that during a limb observation even the top detectors can 'see' lower parts of the atmosphere and possibly even the ground. A FOV-averaging method has been incorporated into the retrieval process. This method also takes into account rotation of the FOV (i.e., when the detector array was rotated from its normal position) for limb observations.

To correct for the problems of inaccurate FOVs a procedure is integrated into NEMESIS. The following correction procedure was applied: Firstly, the FOV response

Table 1: Parameters, radii (in µm) and variances for dust and water ice from Kleinböhl et al. (2011).

Aerosol type	a	b	c	r_{eff}	v_{eff}
Dust	2.24	8.04	0.647	1.06	0.3
Water ice	12.6	31.4	0.436	1.41	0.15

of the detectors is corrected for rotation about the boresight (in the azimuth/elevation plane). Secondly, the corrected FOV response is convolved with the radiation from the scene and then integrated over all possible viewing angles to give the final FOV-averaged radiance. Accurate curves of FOV response in both the horizontal and vertical directions were obtained from laboratory measurements made of detectors during testing prior to launch (McCleese et al., 2007). Further details of this procedure are given in Lolachi (2019).

For forward modelling, the measured individual B2 detector filter bandpasses are used (McCleese et al., 2007), the pale red lines shown in Fig. 1 (see §2.2).

3.3. Sources of Opacity

Two sources of opacity needed to be considered for radiative transfer simulation of the Martian atmosphere: spectral lines and aerosols. Modelling of spectral lines, for carbon dioxide and water, uses line data from the HITRAN 2004 molecular spectroscopic line database (Rothman et al., 2005) and the line-broadening procedure outlined in Kleinböhl et al. (2009). These models are then used to create k-distribution tables. Similarly, for aerosols we follow the procedure outlined in Kleinböhl et al. (2009), to model the dust and water ice aerosols using Mie theory with the modified-gamma distribution (Wolff and Clancy, 2003).

$$n(r) \sim r^a e^{-br^c} \tag{2}$$

where n is the number of particles with radius r, and a, b and c are distribution parameters. We use the parameters and their respective radii and variances from Kleinböhl et al. (2011) (Tbl. 1).

Following Kleinböhl et al. (2009) we use refractive index data from Wolff et al. (2006) for dust along with scaled basalt refractive indices (560–780 cm^{-1}) and data in the far infrared (~380 cm^{-1}) based on Hansen (2003). For water ice refractive indices we use the newer values from Warren and Brandt (2008) rather than the those of Warren (1984) that were used in Kleinböhl et al. (2009, 2011).

For this study, aerosols are assumed to be entirely absorbing (i.e., extinction cross-section equals absorbing cross-section with single-scattering albedo of zero) as the effects of scattering in the thermal infrared are small due to the low optical depths at these wavelengths (Kleinböhl et al., 2009). Though NEMESIS is capable of handling scattering calculations in forward modelling it is incredibly computationally expensive. For one profile, a non-scattering calculation takes ≈30 s while the equivalent scattering calculation took >4 h. Given the volume of data in this study it was not feasible to include it.

Comparison testing between scattering and non-scattering forward modelling was performed to gauge its resulting impact on water vapour abundance. It revealed that at an altitude of 16 km (a region in the atmospheric profile where the water vapour VMR is high) a 5% excess radiance error corresponds to a 10% excess water abundance error, and for a 10% radiance error a 24% abundance error. The excess radiation due to scattering in B2 in the lower atmosphere is generally less than 5% and so the error is comparable to the ~10% error due to the line data meaning our water retrievals should not be overly affected. See Lolachi (2019) for further details.

3.4. Assumption of Local Thermodynamic Equilibrium

For this work we assume the Martian atmosphere is in Local Thermodynamic Equilibrium (LTE). The strongest CO_2 vibrational bands are in LTE in the lower and middle atmosphere up to ≈80 km (Kleinböhl et al., 2009); above this the assumption starts to break down. As the focus of this work is the retrieval of water vapour which is confined well below 80 km this assumption is deemed reasonable. Even so the actual error in temperature at these high altitudes is small, of the order of 2–4 K (Kleinböhl et al., 2009).

4. Sensitivity Studies

As a part of this work an extensive campaign of sensitivity studies were undertaken to assess the viability of vertical water vapour profiles. Full details of these are given in Lolachi (2019) with a brief summary of the work and results given here.

It was originally envisioned that MCS would use the B2 and B3 channels together, using their radiance ratio, to perform the retrievals of water vapour by isolating it from the effects of aerosol (see §2.2). Both channels failed to meet their original specifications and have spectral bandpasses that are significantly wider than designed. A number of simulation tests were performed to gauge the sensitivity of the wider channels to see if they could still be used together or if a different retrieval methodology ought to be sought.

Simulations of individual B3/B2 detector pair ratios found no detectable change in ratio above noise, as the amount of water vapour in a model was varied for a northern hemisphere summer atmosphere (if working as intended the radiance ratio between equivalent pairs of B3 and B2 detectors would change in proportion to the water vapour present). This was for vertical water profiles with a column abundance range of 1–100 pr. µm, representing the full range of water vapour abundances on Mars. Reduced ratio sensitivity was confirmed for scatter plots of B3-B2 radiance from a 4 h block of MCS results when compared with an equivalent simulation of MCS performing nominally, i.e. filters with no broadening. Further simulations tested the effect on the ratio of changing temperature and dust in comparison with changes in water vapour abundance. It was found that low temperatures and more importantly dust opacity both acted to reduce sensitivity of the ratio. For a northern summer equatorial scenario (water column abundance 11 pr. µm) with a typical dust value of τ_{1075}=0.1 (column optical depth at 1075 cm^{-1}, a standard dust measure for Mars, Smith, 2008; Forget et al., 2005, 2006) the reduction in ratio was significant. Increasing the opacity to τ_{1075}=1.8 decreased ratio sensitivity to near-zero. The results of these tests showed that the use of the B3/B2 ratio for water vapour retrievals independent of aerosol is not feasible.

As a consequence of the above the B2 channel must be used on its own in a two-stage water vapour retrieval. This is challenging as B2 is sensitive to both aerosol and water vapour. This fact was suggested by B2 radiance residual tests which sought to gauge the sensitivity of the channel to water vapour. In this test vertical profiles of temperature and dust were retrieved from MCS data. These results were then used as input for a forward model where atmospheric water vapour content was artificially set to zero. The resulting modelled B2 radiances were subtracted from the corresponding real observations to create B2 radiance residuals. If there was nominal sensitivity, the radiance residuals should map to where water vapour was present qualitatively, as radiance contributions from other factors such as dust in B2 would be subtracted out. Although, a crude approximation of the water vapour presence was seen where expected, though there were also several anomalies, including negative residuals which indicated that factors other than water were affecting the radiance in the channel. One such factor was sensitivity of B2 radiances to water ice, the effects of which had not been included. Subsequent simulations of the effect of dust and ice on B2 radiance confirmed that the channel has significant radiance contributions from aerosol when present.

A final set of retrieval simulations were used to establish the effect on water vapour retrieval accuracy of aerosol opacity and the incorrect choice of aerosol size mode (distribution), i.e. using the wrong extinction cross-section at B2. For these tests, model atmospheres were used in conjunction with a forward model (part of the NEMESIS suite) to generate synthetic MCS measurements with noise added. A two-stage retrieval was then performed on the synthetic measurements with temperature and aerosol retrieved in the first stage and water in the second (similar to that described in Section 5). For the second stage, the vertical profile water vapour retrievals were repeated three times for each set of synthetic MCS measurements (i.e., one model atmosphere), using three different *a priori* profiles where VMR was constant with height. These were for ‘low’ (VMR=10^{-7}), ‘medium’ (VMR=10^{-5}) and ‘high’ (VMR=10^{-3}) VMR amounts. These profiles would create ‘brackets’ that could test for retrieval sensitivity. Where there is information in the retrieval the three retrieved profiles will converge, while elsewhere they will relax towards their initial *a priori* values (see Fig. 2).

The tests were conducted for a range of opacities and aerosol size modes using

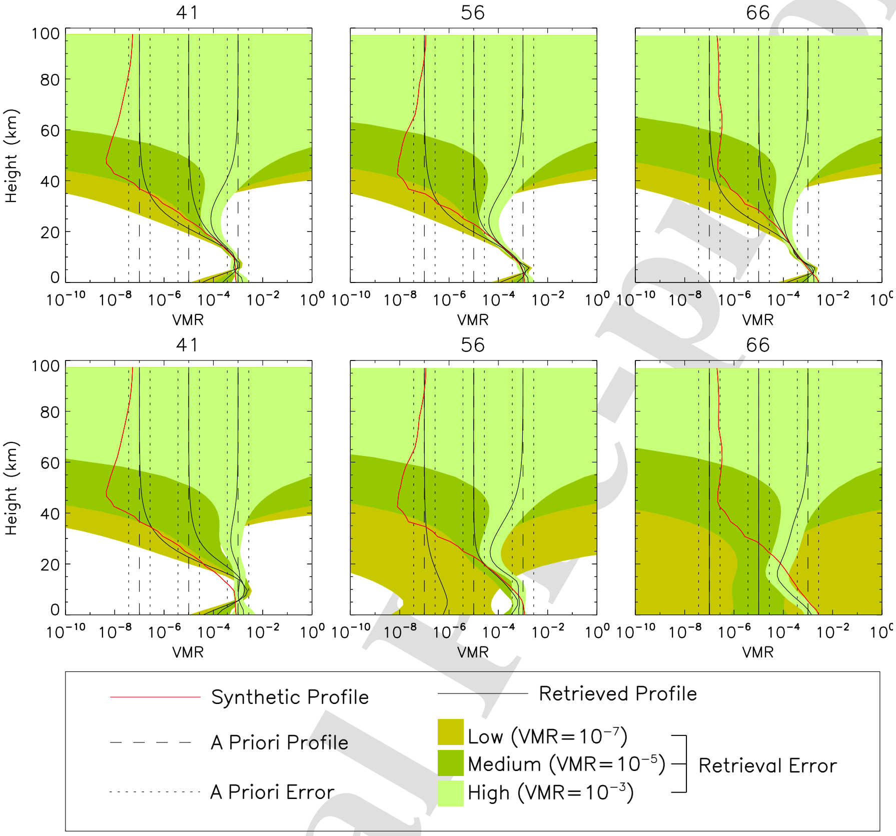

Figure 2: Sample bracket water retrievals simulation for cases where simulated atmosphere is generated with water ice particles with r_{eff}=4.0 µm: (**Top**) Water ice column optical depth τ_{A4}=0.01 (**Bottom**) Water column optical depth τ_{A4}=0.1. Results are shown for three model atmospheres, labelled 41, 56 and 66. For each model atmosphere retrievals are performed for low, medium and high VMR cases (black dashed lines). All cases retrieved assuming r_{eff}=1.41 µm, i.e., incorrect size mode. Where the retrieved profiles (black solid lines) converge on the the synthetic model profile (red line) indicates retrieval sensitivity. Errors for *a priori* and retrieved profiles are given as black dotted lines and green shaded regions respectively. In models of lower opacity (top), retrievals converge pretty well, despite retrieving with the wrong aerosol size mode. For models of high optical depth (bottom) problems emerge and the retrievals produce false results, produced by the retrieval mistakenly attributing B2 radiance absorption/emission from water ice to water vapour. This manifests as offsets in the retrieved profile from the true profile.

gamma (Hansen and Travis, 1974) and modified-gamma particle size distributions (see §3.3). These opacities are representative of condition on Mars during the northern hemisphere summer season. Sets of dust/ice particle size distributions were chosen to reflect a range of conditions on Mars based on the work of Wolff & Clancy (2003), Wolff et al. (2006) and Kleinböhl et al. (2009, 2011). Northern hemisphere dayside atmospheres during summer were modelled as this season and region corresponds to the highest water abundances on Mars and so those most readily detectable, as well as the timing of the retrieval results presented in Section 6. Temperature and water vapour profiles were taken from the Mars Climate Database (MCD, see §5.1). Dust profiles were constructed using a Conrath profile shape with an inflection coefficient of 0.007 (Conrath, 1975). For water ice, profiles were extracted from the MCD and then scaled to the required optical depth.

These tests gave a benchmark to give an idea of the conditions under which retrievals would succeed. It was found that increasing either aerosol opacity or the difference between the retrieved and modelled aerosol size mode reduced retrieval accuracy. Combinations of high opacity and high model-retrieval size mode difference gave the worst results.

When there is a mismatch between retrieval/model aerosol modes this can manifest itself with a systematic offset of the retrieved profile from the true model profile, the effect becoming more prominent as the difference between the retrieval and model aerosol modes increases (see Fig. 2). This is due to additional/missing aerosol radiance in B2 because of the difference in extinction cross-section between the model/retrieval modes at B2, which is misinterpreted by the retrieval as extra/less water vapour.

For cases tested where only dust is present, when retrieved with a dust mode of r_{eff}=1.06 µm, good results were obtained for dust opacities up to τ_{A5}=0.075 (column optical depth at A5). This held true when the model dust mode was varied (i.e. retrieving with wrong mode) up to r_{eff}=1.8 µm. For cases of τ_{A5} ≤0.025, the effect of the dust mode is less important.

For the ice series tests, atmospheres were modelled with both dust and ice present; dust was held fixed at τ_{A5}=0.025. When retrieved with an ice mode of r_{eff}=1.41 µm good results were obtained for ice opacities up to τ_{A4}=0.075 (column optical depth at A4). This continued to hold when varying mode ice mode from r_{eff}=1.0 μm up to r_{eff}=2.0 μm. For cases of τ_{A4} ≤0.025, the effect of the ice mode is less important. When both dust and water ice are retrieved extra degrees of freedom are introduced to the retrieval and this can lead to difficulties in 'tuning'.

Optimal estimation retrievals must be tuned to provide a suitable solution. This is done by weighting the solution between the *a priori* and the measurements using the errors on each (Lolachi, 2019; Rodgers, 2000; Irwin et al., 2008). Weighting too strongly towards the measurements (by having small measurement errors and large *a priori* errors) tends towards an exact solution that has unrealistic high frequency perturbations, despite giving small retrieval errors. Weighting too far towards the *a priori* (small *a priori* errors and large measurement errors) means the retrieval is smooth, but has no information from the measurements. Therefore, there is a trade-off between unrealistic high-frequency perturbations and vertical smoothing to get a suitable inversion (Rodgers, 2000; Irwin et al., 2008).

The different *a priori* and the relative proportional errors used result in differing retrieval sensitivities to dust and ice, which may result in an imbalanced tuning at the higher opacities and larger incorrect ice modes. These cause unpredictable effects on the water vapour retrieval as first stage retrieval errors are propagated into the second stage.

When compared with values for this season from the MCS Level 2 (L2) Retrievals (Pipeline Version 4.3.3) dataset performed by Kleinböhl et al. (2009) (more detail on the L2 data in the next section), it was found that most dust and water ice column opacities for dayside measurements fell within the 'good results' range described above, implying a good chance of retrieval success with real data.

5. Retrieval Method

5.1. A Priori

Optimal estimation retrieval algorithms like those used in NEMESIS require the provision of an *a priori* model atmosphere to provide a first-guess along with constraint and smoothing for the resulting profiles (Irwin et al., 2008; Irwin, 2009). For this work, *a priori* atmospheres are constructed using a combination of the MCS L2 retrievals dataset (see above) and the Mars Climate Database (MCD) Version 4.1 (Forget et al., 2006). The primary source for constructing a model atmosphere is the L2 dataset, however these retrieved profiles do not always cover the full height range necessary (see below). The retrieved quantities are only reported for levels where sufficient information could be extracted from the radiances; other levels are marked as 'missing'. Consequently, 'missing' values are substituted with extrapolations, either based on MCD data or other suitable scaling relations (see below).

From the MCS L2 database retrieved vertical profiles were used for temperature, dust opacity at A5 in km^{-1}, ice opacity at A4 in km^{-1} along with their respective errors along with retrieved pressure and surface temperature. From the MCD we used data from the baseline 'MY24' (Martian Year 24) scenario based on assimilation of TES observations in 1999–2001: temperature profiles, surface pressure, dust column opacity, water vapour and ice (column and mixing ratio), N_2 and CO_2 volume mixing ratios capturing seasonal and diurnal variation.

The advantage of the L2 dataset is that it gives an obvious starting place for our retrievals given that that they are based on the same observations for the same instrument. This simplifies the creation of the *a priori* and gives a likely accurate place to start from. Use of MCD data as a stand-in for missing data is justified given that the Mars GCMs source data used to construct the database have been extensively validated with observational data (Forget et al., 2006) and the observed repeatability/stability of the Martian climate cycles (Smith, 2008; Montmessin et al., 2017a).

The model atmosphere is constructed with 39 altitude levels that are equally spaced in log p (pressure) and covers a height range of 0–100 km; the L2 or MCD profiles are interpolated onto this grid. The choice of using log p as opposed to equal spacing in either pressure or height is justified by its resulting computational expediency. This is because it provides higher resolution (i.e. more closely spaced layers) in the lower atmosphere where variables such as temperature, pressure, composition etc. may change rapidly with height, whereas in the upper atmosphere it provides lower resolution (i.e. more widely spaced layers) where atmospheric variables change more smoothly. This results in fewer wasted calculations and so makes the overall calculation more computationally efficient. The atmosphere is constructed using the following variables:

Temperature/Pressure Surface values and vertical profiles above the surface.

Gases: CO_2, N_2 and Water Vapour Vertical profiles of volume mixing ratio. For CO_2 and N_2 these are uniformly mixed to the top of the atmosphere with values of 0.9532 and 0.027 respectively. For radiative transfer modelling N_2 is treated as being spectroscopically inert and is included for composition/pressure purposes only. Water vapour varies massively spatially and temporally.

Aerosols: Dust and Water Ice Clouds Vertical profiles of specific concentration are constructed in units of number of aerosol particles per gram of atmosphere (g^{-1}). Vertical L2 aerosol optical depth profiles requires conversion for use (see below).

Temperature and pressure vertical profiles along with surface temperature L2 data are used where available with MCD values being used directly or in extrapolation of missing values. For vertical profiles of dust and water ice specific concentration, extrapolations were scaled based on the top and bottom values of these profiles. Extrapolations have to be made in order to have have full *a priori* profiles for conducting retrievals which are explained next. Extrapolated values at heights between the ground and the bottom of the L2 profile are referred to as lower values and those above the L2 profile (up to 100 km) are upper values.

For the missing upper/lower pressure values, an exponential drop-off with a scale height of 10.8 km is used. For the lower temperature profile values, the values from an equivalent MCD profile are taken and scaled and shifted such that the the temperature at ground level of the extrapolated profile matches the MCD value and the top value matches the bottom of the L2 data. For upper values, a constant temperature shift of the MCD profile at the extrapolated heights to match the top of the L2 profile is used. Typically this corresponds to a lower extrapolation range of 0–10 km and 85–100 km for upper values.

For aerosols the opacity profiles from the L2 data need to be converted into units of specific particle density, g^{-1} (particles per gram of atmosphere) for use in NEMESIS.

This is done with the equation:

$$N(z) = \frac{\Delta\tau_{\mathrm{L2}}(z, \nu)}{\rho(T(z), p(z)) \cdot \sigma_{\nu}^{ext} \cdot \Delta s} \tag{3}$$

where $N(z)$ is the aerosol specific concentration at height z, $\Delta\tau_{\mathrm{L2}}(z, \nu)$ is the limb extinction drop over a kilometre at wavenumber ν, $\rho(T(z), p(z))$ is the atmospheric density at z as a function of temperature, T and pressure, p, σ_{ν}^{ext} is the extinction cross-section at ν and $\Delta s = 1$ km. The value of ν for dust profiles is 463.510 cm^{-1} (centre of A5 channel) and 843.394 cm^{-1} for ice (centre of A4 channel).

For the dust profile, missing lower values are replaced with a profile that is constant with height, equal to the specific concentration value at the bottom of the L2 profile. This process is mirrored for missing upper values in dust and ice, but at a minimum value of 1 g^{-1}, a zero equivalent abundance (a negligible amount in NEMESIS, as it cannot handle zero due to calculating using logarithms of abundances). For the ice profile, lower values are extrapolated via an exponential decay below the bottom L2 value using a scale height of 1.25 km. This scale height was chosen to match observed profile decay observed in more complete L2 profiles. For dust and ice this typically corresponds to a lower extrapolation range of 0–10 km. The upper range is normally above approximately 30 km for dust and 40 km for ice.

For surface temperature and pressure retrievals L2 data were used where available, otherwise the MCD data served as fallback. For retrievals with no nadir radiances surface temperature was not retrieved. Water vapour VMR profiles are taken directly from the MCD.

5.2. Comparison of L2 Method with Optimal Estimation

The L2 retrievals of Kleinböhl et al. (2009) were performed using a modified form of the Chahine retrieval algorithm (Chahine, 1970, 1972). The NEMESIS optimal estimation and L2 retrieval methodologies have a number of significant differences. Optimal estimation can be described as a constrained matrix method, while the L2/Chahine method is an unconstrained general relaxation method (Puliafito et al., 1995). The constraint in optimal estimation comes from the use of the *a priori* which provides additional information to the retrieval, not available to the the L2/Chahine method. The *a* *priori* also provides smoothing which helps remove unrealistic oscillations introduced by over-fitting to the noise. The L2/Chahine method does not have this and instead has to manually apply smoothing to get rid of ripples caused by the weighting functions and remove oscillations.

In addition, through the use of the covariance matrices, optimal estimation provides an intrinsic error analysis that takes account of errors from various sources: *a priori* profile errors, forward modelling errors, smoothing errors and measurement errors (noise) (Rodgers, 2000). Including these contributions it is able to provide a quantitative total retrieval error. The L2/Chahine method cannot do this and has to resort to either: a) manually perturbing atmospheric quantities level by level in the state vector and running a radiative transfer calculation for each to see the impact, which increases computational expense or b) making approximations of this perturbation process to save time at the expense of error accuracy.

As a result of all the above, optimal estimation is likely to offer a distinct advantage in regions of the atmosphere with low information content. In these regions the L2/Chahine method is prone to over-fit to the measurements, due to the lack of additional constraint and smoothing. In contrast, the optimal estimation retrieved profile will be smoother and gradually relax back towards the *a priori*, resulting in a lower total retrieval error and potentially extending the ‘useful’ altitude range of the retrieved profile. Evidence of this can be seen in the results of Puliafito et al. (1995) who compared five retrieval algorithms including optimal estimation and the Chahine method using measurements and simulations of the Millimetre-Wave Atmospheric Sounder (MAS) flown on spacelab shuttle missions. Their study also indicated that both methods gave similar answers in regions of the atmosphere with high information content.

5.3. Detector Selection

For limb observations, as the tangent height is lowered the amount of absorption along limb paths increases, eventually leading to paths becoming optically thick. This is problematic as it means that as the optical depth increases the region of atmosphere being sounded moves closer to the spacecraft. Consequently, each channel’s detector is sounding the atmosphere at different horizontal distances along the limb path where atmospheric conditions (e.g., temperature, aerosol abundance) may be different, so the resulting measurement is no longer a true vertical profile for a given location. In the worst cases this lowers retrieval accuracy and so it becomes necessary to remove these detectors from the retrieval. This is less of a problem for nadir observations, even in the optically thick case, as all detectors are looking straight down, 'seeing' the same ground position and hence the same region of atmosphere. Additionally, as nadir viewing paths are shorter the chances of the atmosphere becoming optically thick at the channel's wavelength are much lower. As the lines-of-sight for all detectors in nadir viewing are almost identical, detector radiances are channel-averaged for use in the retrievals.

For A1–A5 the retrieval uses the same limb observation detectors as those used in L2 data (they are not altered during the course of the retrieval). Full details of the selection process for these channels are given in Kleinböhl et al. (2009). Firstly, the bottom detectors in each channel are removed where hot ground can contaminate the measurement due to the wide FOV detector response. Secondly, detectors are removed that have exceeded limb opacity thresholds for the relevant channel. For A1–A3, detectors are removed if they contain insufficient signal and there is a non-opaque alternative. Finally, for A4 and A5, the highest detectors used need to exceed radiance thresholds to avoid low radiances from FOV wing misrepresentations being falsely interpreted as aerosol. The criteria described above were applied at the time when these retrievals were made and are deemed valid for use in this retrieval as there is no good reason to think that our first stage retrievals will vary significantly from the L2 profiles. In the second stage, only the B2 channel is used and limb detectors with a boresight altitude below 1 km are removed to minimise errors due to FOV surface contributions. This corresponds to a bottom detector boresight altitude in the 3–5 km range, which given the ≈5 km nominal FOV means the surface should not be present, though there may be contributions from the wings (see §3.2).

5.4. Retrieval Procedure

Retrievals from MCS observations were performed with NEMESIS in two stages. Following the procedure outlined below:

Stage 1: Using the *a priori* model a retrieval is performed for temperature, pressure, dust, water ice and surface temperature using channels A1–A5. When retrieving vertical continuous profiles, off-diagonal elements (representing cross-correlation) of the covariance matrix decrease from the diagonal according to l_c, the length scale in units of $\ln p$ over which the inter-level correlation drops off by $^1/_e$ i.e., units of scale height (Irwin et al., 2008; Rodgers, 2000); this controls vertical smoothing. Continuous profiles are retrieved for temperature and aerosols with 'correlation length', l_c=1.0. This value is approximately twice the vertical resolution of limb data and so ensures no structure is present which is not supported by the data. The pressure retrieval is performed for pressure at a single altitude which is then used to scale the rest of the pressure profile accordingly. The altitude used is that from the equivalent pressure retrieval in the L2 data, with the *a priori* error set to the error in the retrieved L2 value. The *a priori* errors for other first stage retrieval parameters are as follows: 2 K for temperature profile and surface temperature, 50% of the specific particle density (particles per gram of atmosphere) at each height for the dust profile and 50% for the water ice profile. Errors in modelling, due to assumptions and approximations made, such as inaccurate line data (and using correlated-k), instrument calibration, pointing, and cumulative errors (from the two-stage retrieval procedure) are bundled into an estimated radiance error known as the 'forward modelling error'. This is added to the channel Noise Equivalent Spectral Radiance (NESR) values to give total *a priori* error (Irwin et al., 2008). A forward modelling error of 0.25 mW/m^2/sr/cm^{-1} is used for channels A1–A5.

Stage 2: Atmospheric parameters retrieved in Stage 1 are used to set the atmospheric state for the water retrieval. Additionally, errors from stage one are propagated into stage two. The MCD water vapour data are used as the *a priori* profile with an *a priori* error of 50% in the VMR at each height. A continuous profile retrieval is performed for water vapour using the B2 channel with l_c=1.0 and a forward model error of 0.25 mW/m^2/sr/cm^{-1}.

6. Results

6.1. Retrieval Quality and Coverage

A key signifier of retrieval quality is the χ^2/n_y value, where χ^2 is the chi-squared statistic and n_y is the number of points in the measurement vector. The χ^2 function describes the closeness of fit of the measured radiances to the calculated ones as

$$\chi^2 = (\mathbf{y} - \mathbf{F}(\hat{\mathbf{x}}))^{\mathrm{T}} \mathbf{S}_{\epsilon}^{-1} (\mathbf{y} - \mathbf{F}(\hat{\mathbf{x}})), \tag{4}$$

where **y** gives the measurement vector (including noise), $\mathbf{F}(\hat{\mathbf{x}})$ gives the modelled radiances for the model state vector $\hat{\mathbf{x}}$, and $\mathbf{S}_{\epsilon}$ is the measurement error covariance matrix (containing both noise and forward modelling error, Irwin et al. 2008).

It is important to note that, though the χ^2/n_y is very similar in form, this statistic is not the reduced chi-squared, χ^2/n_f, where n_f is the number of degrees of freedom. This is because there are not n_y independent data (degrees of freedom), i.e., $n_y \neq n_f$. The χ^2/n_y statistic is useful for analysing the fit quality for the manual quality control process described here. Under normal circumstances it is $O(1)$ (i.e., within an order of magnitude) for a realistic converged solution.

Additionally, the χ^2/n_y metric, must be distinguished from the cost function, ϕ, in Eq. 1. Firstly, χ^2/n_y is only generated as a retrieval output to indicate the closeness of fit, but is not actively used in the retrieval. Whereas, ϕ is actively used in the iterative process of the retrieval (see §3.1). Secondly, χ^2/n_y only measures the difference between the modelled and measured radiances, but ϕ contains the additional *a priori* constraint term.

A χ^2/n_y=1 threshold was set for all first stage retrievals while for the second stage retrievals a χ^2/n_y=3 value was used for the dayside observations and χ^2/n_y=1 for the nightside results. The thresholds for first stage and second stage are linked, so that results have to pass both thresholds in order to be included (e.g., a dayside first stage retrieval that had χ^2/n_y=0.9 with corresponding second stage χ^2/n_y=5 would not be included). These criteria ensure that the retrieved profiles fit the data to within measurement errors.

For northern hemisphere dayside observations, i.e., those with the highest water abundances, it was impossible to get χ^2/n_y values lower than 2–3. For dayside observations, testing by inspection with small subsets of data showed that this gave good radiance fits and a large fraction of non-spurious results. An example dayside retrieval is shown in Fig. 3. To assess information content, we construct an improvement factor, $\mathbf{c_i}$, which is defined as:

$$\mathbf{c_i} = 1 - \left(\frac{\mathbf{S_n}(i,i)/\mathbf{x_n}}{\mathbf{S_a}(i,i)/\mathbf{x_a}} \right) \tag{5}$$

where $\mathbf{x_a}$ and $\mathbf{x_n}$ are the *a priori* and retrieved value state vectors of water vapour vertical distribution; and $\mathbf{S_a}(i,i)$ and $\mathbf{S_n}(i,i)$ are the diagonal elements of the corresponding error covariance matrices. As the elements of $\mathbf{S_n}(i,i)$ decrease, $\mathbf{c_i}$ approaches one. The improvement factor is an indicator of where information is found in a retrieval, with values closer to one indicating more information.

In the nightside results, for the equivalent northern hemisphere high water abundance region, many retrieved profiles were found to have χ^2/n_y<1. Initially, the same χ^2/n_y=3 threshold was tried as for the dayside results, but this led to the inclusion of a large fraction of spurious retrievals.

Unfortunately, filtering results by χ^2/n_y alone is not sufficient to guarantee the removal of spurious retrievals. Spurious retrievals are present in both the dayside and nightside results. Curiously, the problem is much more severe for the nightside results despite generally having lower values of χ^2/n_y. These spurious retrievals take the form of unrealistically exaggerated and oversaturated (by factors of 100 or more) water vapour layers. They are normally co-located in altitude with dust or water ice layers. It is thought that these spurious layers are due to aerosol radiance contribution in B2 being misinterpreted by the retrieval as water vapour. This suggests errors in the extinction cross-sections in the far infrared at B2. These could be caused by either by an inappropriate choice of particle size distribution or errors in the complex refractive index data at these wavelengths. Consequently, this is likely to lead to problems at higher aerosol opacities. This matches the behaviour seen in the sensitivity simulations of Section 4. The nature of these spurious cases and potentially genuine cases of water vapour layers in excess of saturation, is further discussed in §6.4.

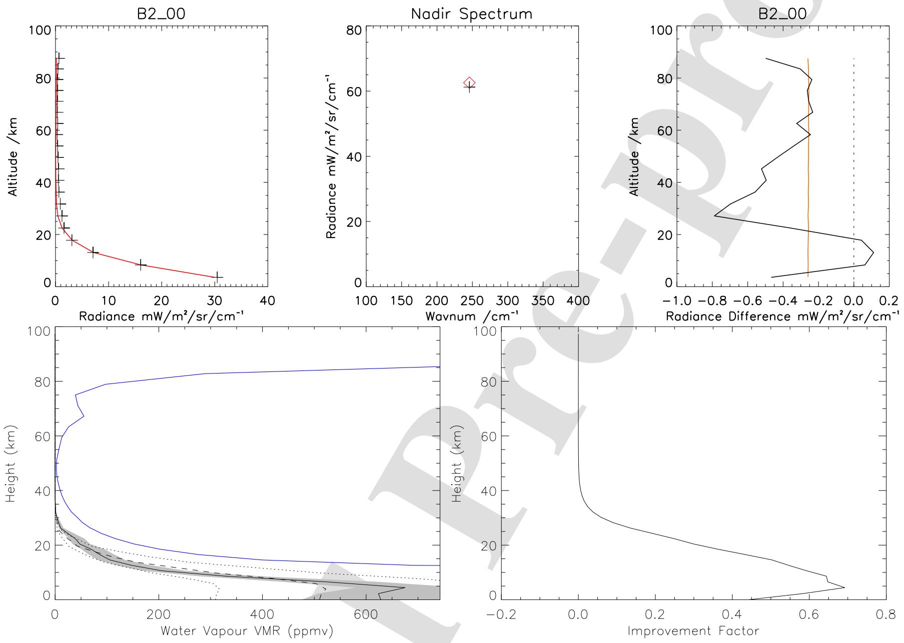

Figure 3: B2 Filter Radiance Fits & Retrieval for N. Mid-Latitude Dayside Water Retrieval:**(Top Left)** Limb radiance fits where the red line corresponds to retrieved radiances and the black crosses indicate observed radiances, **(Top Middle)** nadir fit. **(Top Right)** difference between observed and retrieved limb radiances (black line) with radiance error including forward modelling error (orange line). **(Bottom Left)** Retrieved water vapour profile as black solid line with grey shaded error. The *a priori* profile and error are the dashed and dotted lines respectively and the blue line is the saturation VMR. **(Bottom Right)** improvement factor showing where information is present in the retrieval. **Profile Information:** *Date:* 1 October 2006; *Spacecraft Clock Time:* 844145475.464 s; L_s: 114.25°; *LST:* 15.118 h; *Limb Observation Location:* 51.098°N, 85.420°W; *Nadir Observation Location:* 51.432°N, 85.669°W.

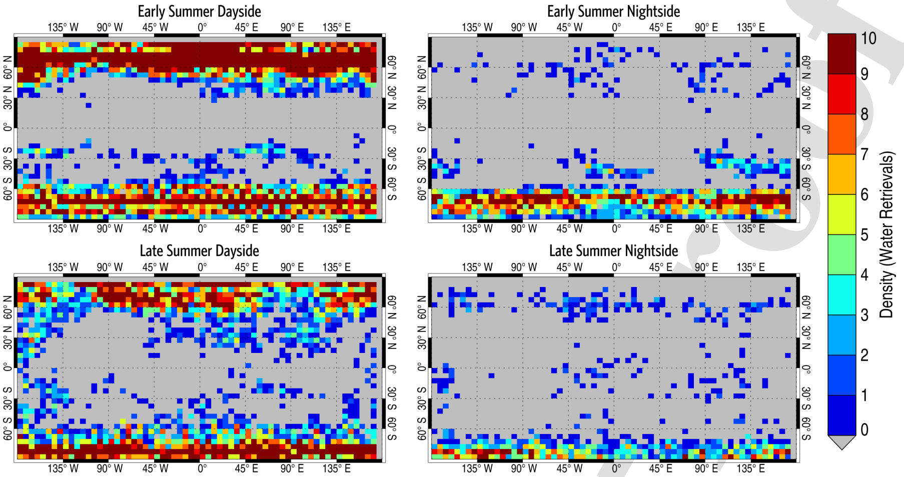

Figure 4: Number of retrievals per bin for early/late NH summer dayside and nightside result blocks after thresholding by χ^2/n_y (see text for details). Dark red bins have ≥10 retrievals. Coverage for the dayside is better than nightside especially in the NH. This is due to the stricter thresholds required for nightside observations (see text for details). The large gap in observations in equatorial regions and northern tropics is due to high dust and water ice opacities in this region making retrieval success unlikely.

Retrieval coverage for each block is given in Fig. 4. Coverage for dayside results is much better than for nightside results, due to harsher thresholds in χ^2/n_y required for the nightside results. In the dayside results, coverage is good between the mid-latitudes and poles for both hemispheres, with better northern hemisphere coverage for the early NH summer dayside results. For the nightside results, northern hemisphere coverage is considerably lower than for the southern hemisphere, with the early NH summer block having better overall coverage than the late NH summer block.

A large gap is seen in the equatorial and northern tropics for all blocks. High aerosol opacities in this region prevent good retrievals from being performed here. For dust this is due to the high equatorial opacities and for water ice high opacities in the equator and northern tropics.

For zonal average plots and histogram map plots retrieved profiles were binned in bins of 5° latitude and 6.25° longitude and 5 km in height. For the zonal average line profile plots the retrievals were binned in bins of 10° latitude. For the line plots a mean profile and the standard deviation were calculated for all of the retrievals in the bin.

6.2. First Stage Retrieval Results

As water vapour is the main focus of this work and for the sake of brevity, zonal averages of temperature and dust opacity retrievals will not be shown. Additionally, the zonal averages for temperature and aerosol opacity are very similar to the seasonal averages given in McCleese et al. (2010) (and canonical results) and so it seems needless to reproduce them here. Early NH summer temperature results show a clear asymmetry with a warmer northern hemisphere, while late NH summer results show a move towards an equinoctial structure that is symmetric about the equator. For dust opacity, our results indicated the highest opacity regions are towards the equator (also seen in McCleese et al., 2010). For the curious reader, full first stage retrieval results and a comparison with the McCleese et al. (2010) results are given in Lolachi (2019). However, we do include our zonal averages for water ice opacity (Fig. 5) as they are needed to show the link between our water vapour results and the aphelion cloud belt through the hygropause/condensation level (see §7.3).

In both the early and late NH summer blocks a strong diurnal variation of tropical water ice can be seen, attributed to the diurnal thermal tide by McCleese et al. (2010). The strongest regions of ice opacity are confined to the equator on the dayside and more spread out on the nightside (and reaching to lower altitudes), the aphelion cloud belt seen in past observations. High equatorial ice opacity for early NH summer dayside results is implied by the empty bins in this region (due to the low likelihood of retrieval success because of the high opacities present), and the elevated opacities on either side. For the late NH summer multiple broad maxima are seen over the latitude range.

6.3. Second Stage Retrieval Results: Column Abundances

Water vapour column abundances were obtained from the retrieved vertical profiles by integrating water vapour VMR over the altitude range. Dayside column abundances for both early and late NH summer blocks are presented in Fig. 6. The nightside results have been left out of this section because the poor coverage gives undue weight to the spurious retrievals and outliers are more prominent in those blocks, leaving little useful information to be gleaned. Column abundances are given for both topography scaled (blue line) and unscaled (red line) cases. The scaled values account for differences in

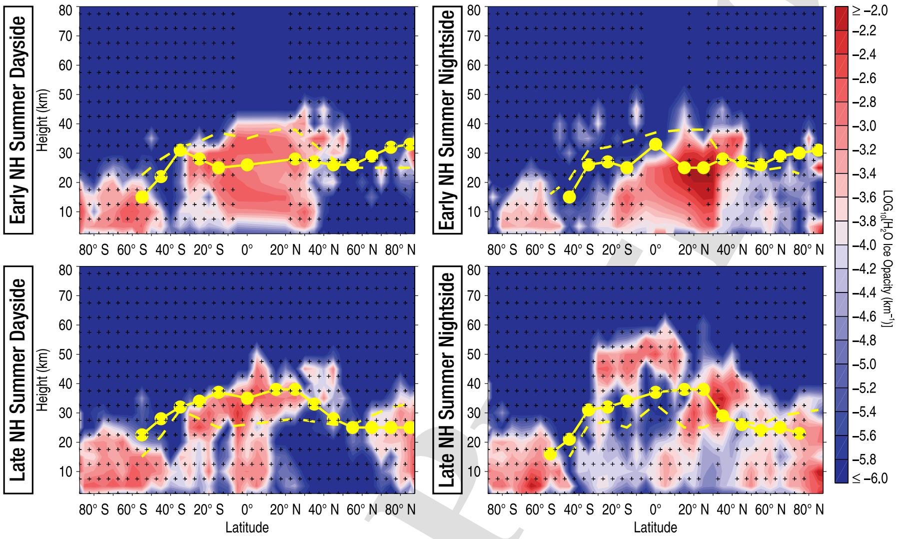

Figure 5: Log$_{10}$ of zonal average water ice opacity (km^{-1}) dayside/nightside retrievals for: **(Top Row)** Early NH Summer and **(Bottom Row)** Late NH Summer. Crosses indicate location of bins that contain retrieval data. (**Solid Yellow Line**) marks the 'profile top', a proxy for the condensation level, discussed in §7.3. Values were calculated using latitude bins from vertical profiles in Figs. 10 and 11. (**Dashed Yellow Line**) shows the profile top from the corresponding season to highlight difference (e.g., in the top left panel the solid line shows the profile top values for the early NH summer dayside and dashed line shows the profile top for late NH summer dayside). The high opacity region near the equator is the aphelion cloud belt. A correlation is seen between the profile top and the strength and location of the cloud belt. Seasonal differences in ice opacity and profile top (condensation level) are clearly visible. During the early summer the profile top is lower in the equator and tropics along with the aphelion cloud belt. In the late summer the profile top is higher in equator and tropics along with a higher and weaker aphelion cloud belt. This supports the idea that seasonal variation in the vertical extent of water vapour is linked with the height and strength of the aphelion cloud belt (see Fig. 15 and §7.3 for details.)

topography and are calculated according to (Smith et al., 2002):

$$d_{\text{scale}} = \frac{d}{(p_{\text{surf}}/6.1)}, \tag{6}$$

where d_{scale} is the topography scaled water vapour column abundance in pr. µm, d is the unscaled column abundance and p_{surf} is the surface pressure in mbar.

For comparison, scaled column abundance data is also shown for TES (Smith, 2008, 2002) and SPICAM (Trokhimovskiy et al., 2015). Zonally averaged TES data taken from Smith (2008, 2002) has been binned over the same L_s ranges as our data and has been averaged over three Martian years within MY24–26 (14h LST average). SPICAM zonal average data taken from Trokhimovskiy et al. (2015) has been averaged over five Martian years (MY27–31) and is given for L_s values of: 111° (14h LST average), 139° (13h LST average), 141° (13h LST average), and 173° (11h LST average). These values of L_s bracket our observations.

Dayside results for both early and late NH summer show an unrealistic large spike in the southern mid-latitudes (highlighted in grey). This is caused by the high number of spurious retrievals and outliers in this band which still pass the χ^2/n_y threshold (i.e., the unphysical supersaturated observations caused by the aliasing of the water signal by aerosol in B2 radiances discussed earlier). This can be seen when looking at the distribution for the same column abundances over latitude and longitude in Fig. 7. Also noticeable here is the dearth of equatorial and northern tropics results for the early NH summer results. However, for the late NH summer block there are some retrievals in this region, though relatively few in number. As explained earlier the reason for fewer retrievals here is that this is a region of high aerosol opacity making retrieval success unlikely. For both early and late summer a less severe version of the spurious retrievals problem seen in the SH causes similar problems at latitudes above 60°N, causing the divergence seen from the TES and SPICAM values. The problem gradually increases moving towards the north pole (indicated by shaded grey gradient region).

Barring these problems zonal average column abundances compare favourably with historical observations such as those of TES (Smith, 2008, 2002), SPICAM (Trokhimovskiy et al., 2015) and ground-based observations (Krasnopolsky, 2015) (not shown). An important metric in the literature for comparison is that of the early NH summer

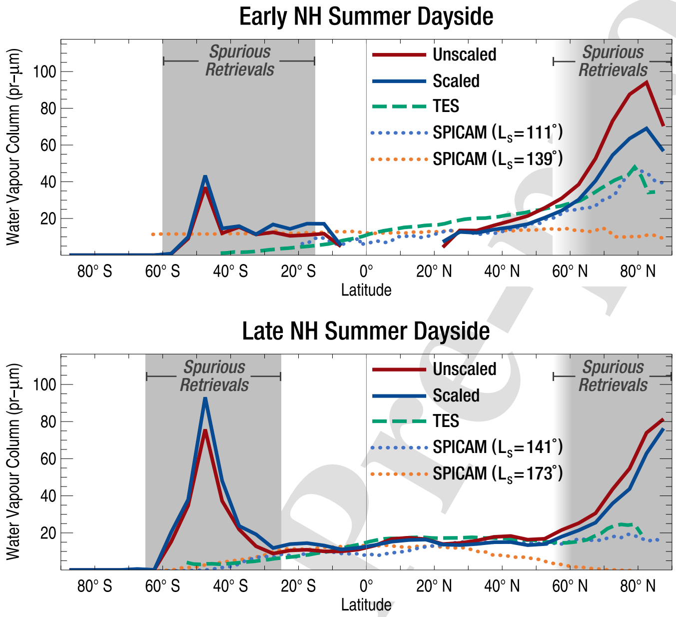

Figure 6: Zonally averaged water vapour column abundances for dayside results: **(Top)** Early NH Summer (L_s=111–140°); **(Bottom)** Late NH Summer (L_s=140–173°). Area highlighted in grey indicates locations of spurious retrievals caused by unphysically supersaturated results which heavily skew the results leading to the unrealistic spike seen in values seen in the SH (see Fig. 7 also). Outside the grey regions up to 60°N values compare favourably with historical observations such as those of TES (Smith, 2008, 2002), SPICAM (Trokhimovskiy et al., 2015) and ground-based observations (Krasnopolsky, 2015) (not shown) with the distinctive NH peak. At higher northern latitudes some divergence is shown, for the Early NH Summer, results are higher than TES and SPICAM values. For the Late NH Summer, the effect is much larger. Both cases are likely caused by some spurious retrievals skewing the results similar to the solid grey shaded area in the SH, but less severely. Their effect gradually worsens going towards the north pole (indicated by grey shaded gradient). Despite this, the fact that the peak has moved further north in later NH summer, resulting in lower column abundances at high northern latitudes indicates a real seasonal change as reflected in the TES and SPICAM data.

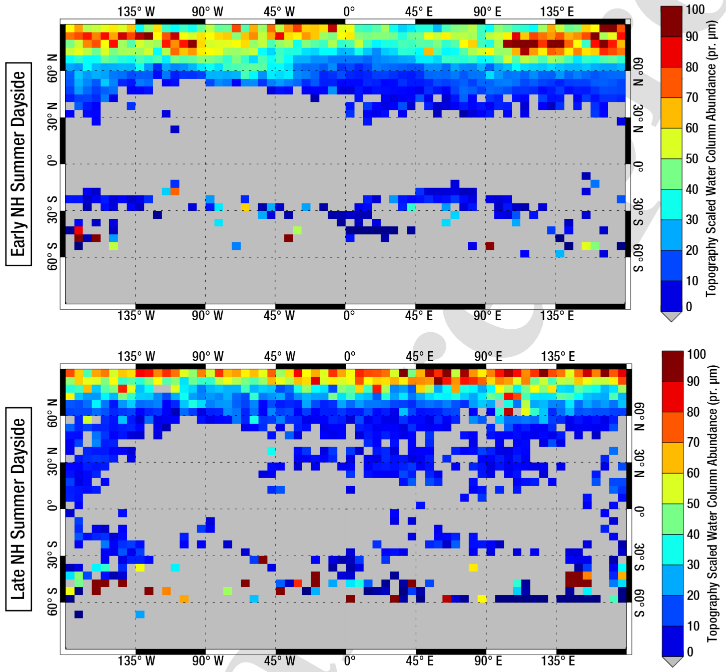

Figure 7: Topography scaled water vapour column abundances for dayside results: **(Top)** Early NH Summer and **(Bottom)** Late NH Summer. Bins containing a high number of spurious retrievals not removed by χ^2/n_y thresholding are seen in the SH as brightly coloured squares among the predominantly blue regions. Note in the early NH summer the high abundance regions at north polar latitudes are strongly separated in the early NH summer block, confined in two bands (possibly three), one from 90°E–90°W and a second smaller band at 50°W–0°W. A change in water vapour distribution can be seen between early and late summer, concentrated at high northern latitudes. These distributions match well with the OMEGA polar map results of Melchiorri et al. (2007) and TES results from Pankine et al. (2009).

northern hemisphere peak abundance (when water column abundances are at their highest point in the year). For early NH summer the scaled peak values of 70 pr. µm compare reasonably with the 50 pr. µm peaks of the averaged TES/SPICAM data, and very well with a maximum peak abundance of 68 pr. µm that was seen in the TES data in MY26 at 80°N (not shown). The peak location of 80°N matches well with the TES/SPICAM results. Good agreement with all TES/SPICAM data is seen in the 40–60°N band. In the 10–20°S band the value of 10 pr. µm seen matches well with the SPICAM observations at L_s=139° and reasonably well with the other SPICAM/TES profiles. A good match in the zonal column abundance profile, for the 40–60°N and 10–20°S regions, is also seen with the ground-based results of Fig. 3 in Krasnopolsky (2015), though their results were at L_s=110° (9h LST) and for a single strip at a longitude of 103°W, rather than a zonal average.

In late NH summer, the peak has moved further north and the drop-off to lower values in the northern hemisphere is much steeper. Relatively constant values of 20 pr. µm are seen up to the southern hemisphere spike with near-zero abundances near the south pole. Good agreement with TES/SPICAM data is seen until 60°N as for the early NH summer case. Above this divergence is again seen, caused by a skew from some spurious data. Despite this, the fact that peak has moved further north in later NH summer, resulting in lower column abundances at high northern latitudes indicates a real seasonal change as reflected in the TES and SPICAM data.

Looking at the column abundance maps in Fig. 7 longitudinal changes in water abundance can also be seen between the early and late NH summer result. Notably in the early NH summer the high abundance regions at north polar latitudes are strongly separated in the early NH summer block, confined in two bands (possibly three), one from 90°E–90°W and a second smaller band at 50°W–0°W. It should be remembered that these are temporal averages over ≈54 sols for early summer and ≈61 sols for late summer. Consequently, the water vapour distributions seen here are not ‘snapshots’ in time of a single distribution, but instead suffer from a smearing effect due to motion of the water vapour in that time period (atmospheric circulation, advection, etc.). This means the broad bands of water vapour seen in each plot may actually be several discrete bands that are merged when averaged over time. Concomitantly, bands of low water vapour abundance, such as the one at 0°E–90°E at high northern latitudes seen in early summer must have been constantly low over the time period.

Results from the NH of Fig. 7 can be compared with the OMEGA polar results of Melchiorri et al. (2007) (Figs. 10–12 for early summer) and the TES polar results of Pankine et al. (2009) (Supplementary Fig. 1c for early summer and 1d for late summer). These observations also suffer from a smearing effect, but to a lesser extent given their higher temporal resolution of resolution of 5° (≈10 sols) in L_s. Taking into account the smearing effect, the northern polar region distributions for early summer match well with both the OMEGA and TES results. In those early summer results several smaller northern polar bands of water vapour are distributed over all longitudes changing as the season progresses, except for the 0°E–90°E region of constant low water vapour. In the OMEGA and TES datasets, the low region is not present before L_s=110°. Pankine et al. (2009) attribute it to either a change in atmospheric circulation, or a change in the sublimation rate of the regolith or North Polar Residual Cap.

For late summer only the TES dataset is available for comparison. A more uniform distribution is seen at high northern latitudes, with bands that are less pronounced and the early summer low band at 0°E–90°E has disappeared. In the TES data the season starts with a more uniform distribution of water vapour with less pronounced bands that gradually decrease in abundance as the season progresses. This is consistent with our results.

6.4. Second Stage Retrieval Results: Vertical Water Profiles

Shown in Figs 10 and 11 are the vertical profiles of volume mixing ratio (VMR) in parts per million by volume (ppmv) of the water vapour retrievals. Results have been presented with one figure for dayside results and one for nightside. Each figure includes both early and late NH summer blocks allowing for easy comparison of seasonal changes. Results south of 70°S have been omitted as retrieval information content is very low here and the abundances are near zero so close to the pole.

Profiles for the improvement factor retrieval diagnostic (see Eq. 5), for selected latitude bands from early NH summer, for day and nightside retrievals, are presented in Fig. 12. They give an indication of where information is found in the retrieval.

For sake of brevity, only selected latitude bands are presented in the figure, as these are representative of the surrounding bands and clearly show the relationship between information content and latitude. The same behaviour is seen in the late NH summer retrievals. Retrieval information content is higher and has a larger vertical extent in the warmer NH than in the colder SH, matching abundance and vertical extent of the water vapour profile. The information content is near zero at latitudes south of 60°S, due to the low water vapour content and low radiances (near the noise level), as a consequence of the lower temperatures here. The plots also clearly show how information content drops below 5 km and at high altitudes as the retrieval relaxes back towards the *a priori* at all latitudes.

An important test for the water vapour profiles is to compare adjacent profiles along a single MRO orbit. Since the horizontal sampling is about half the horizontal width (see Fig. 12 in Kleinböhl et al., 2009), in many cases, they overlap significantly and thus consecutive profiles should show very similar water vapour structure, especially above the boundary layer. However, there may be regions where this is not the case due to strong local gradients. A sample group of consecutive profiles is given in Fig. 8. Above 5 km the profiles are seen to be very similar. Larger changes are seen below this, but this is to be expected as these latitudes correspond to the lower slope of the peak in column abundances (Fig. 6). The column abundances seem to follow this trend, starting at steady value of ≈25 pr. µm in profiles 1 and 2 that then gradually increases to 53 pr. µm in profile 5. The outlier here is profile 3, which matched well above the boundary layer, but has a lower than expected column abundance compared with its neighbours. This difference may be caused by local difference in conditions or topography, or may reflect different conditions for the nadir observation that it is paired with. Regardless, the results are encouraging.

From closer examination of the water vapour profile results, the reason behind the spuriously high column abundances becomes apparent. This is in the form of apparent detached water layers (DWL) with very high mixing ratios, often well in excess of the corresponding saturation VMR. Supersaturation in DWL is on its own not necessarily suspicious, as the same phenomenon was seen by Maltagliati et al. (2011a). However, for supersaturation to occur the atmosphere must be clear of dust, as the dust particles

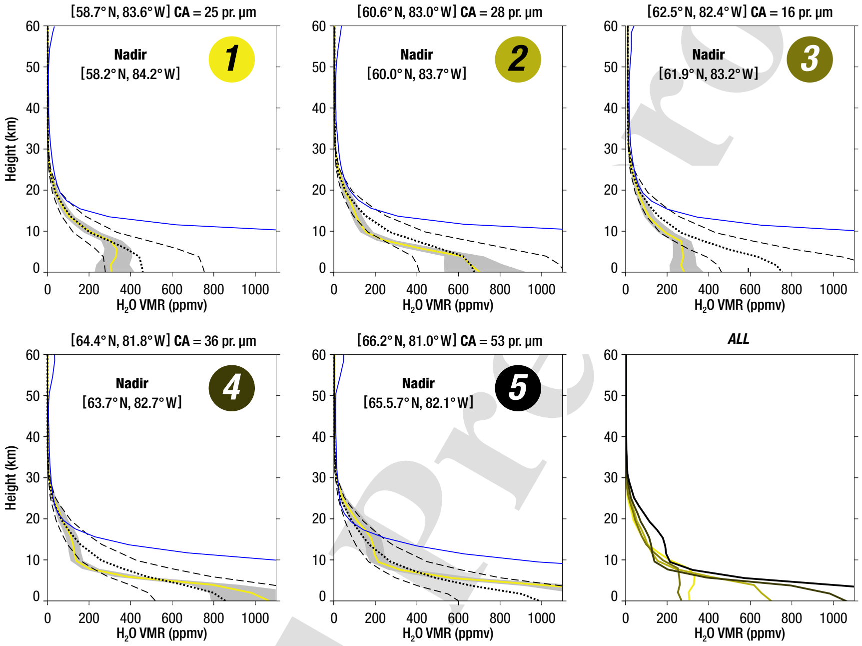

Figure 8: Neighbouring retrieved water vapour profiles (yellow line) along MRO orbit (L_s=114.25°) with error (grey shaded area) and *a priori* (dotted line) with error (dashed line) and saturation VMR (blue line). Location of limb profile is given above each plot along with column abundance. The paired nadir observation location is given in text on the plot. Profiles are identified by number and associated colour, where darkening shade indicates progression in time. All profiles are overlaid on each other for comparison of structure and variation in the 'All' box coloured according to their numbers. Neighbouring profiles along an orbit should show similar water vapour structures, particularly above the boundary layer, with any variation between them being smooth. The increase seen below 5 km, matches the expected trend in increasing column abundance seen in Fig. 6. The outlier here is profile 3, which matched well above the boundary layer, but has a lower than expected column abundance compared with its neighbours. This difference may be caused by local difference in conditions or topography, or may reflect different conditions for the nadir observation that it is paired with. Regardless, the results are encouraging.

function as condensation nuclei for water vapour (Maltagliati et al., 2011a).

When looking at individual profiles in conjunction with the corresponding aerosol profile, for retrievals where some of the more extreme DWL occur, it can be seen that the extreme cases are most certainly spurious. This is because the peaks of the DWL line up exactly with the peak of high-opacity dust and/or water ice layers. It seems probable that with a dust/ice layer of high limb path opacity there will be significant aerosol emission or absorption in the B2 channel which is mistaken for water vapour by the retrieval. An example retrieval is shown in Fig. 9. Here there is a large DWL at around 20 km with co-located dust and ice peaks in specific density. Looking at the observed radiance profile it can be seen there is a radiance ‘bump’ at the location of the peak and this is likely due to dust radiance in the channel. The retrieval fails to match the bump and underestimates radiance here. Below the height of the DWL the water profile radiances fit well and are below saturation, indicating that the rest of this profile is more reliable. This interpretation is supported by the results of sensitivity simulations in Section 4. The offset of the retrieval profile from the true value matches the behaviour seen in aerosol size mode sensitivity study, caused by retrieval using the wrong size mode at high opacities (Fig. 2).

The DWL in our results are mostly present in areas of high aerosol opacity such as the tropics and equator (dust and ice) and polar regions (ice from the polar hood). It is likely that many of these are false retrievals where an additional radiance contribution in B2, from aerosol, has been misinterpreted as a water signal and led to false, overly large, abundances. This is probably because assumed choice of aerosol size distribution is not appropriate in these cases. Additionally, the problem is much more severe in the nightside results and this is likely to be due to the ice particles here being larger than previously thought (Kleinböhl et al., 2017). It should be noted though that the co-location of dust and water do not automatically entail false results. Maltagliati et al. (2013) frequently observed this correlation in their own results.

Ignoring this problem for a moment, we can see that despite this the general expected trend of a very dry winter southern hemisphere (SH), with a much wetter summer northern hemisphere (NH) is seen. This is most notable in the polar regions at the caps where the bulk of the water is released and profiles increase to large amounts

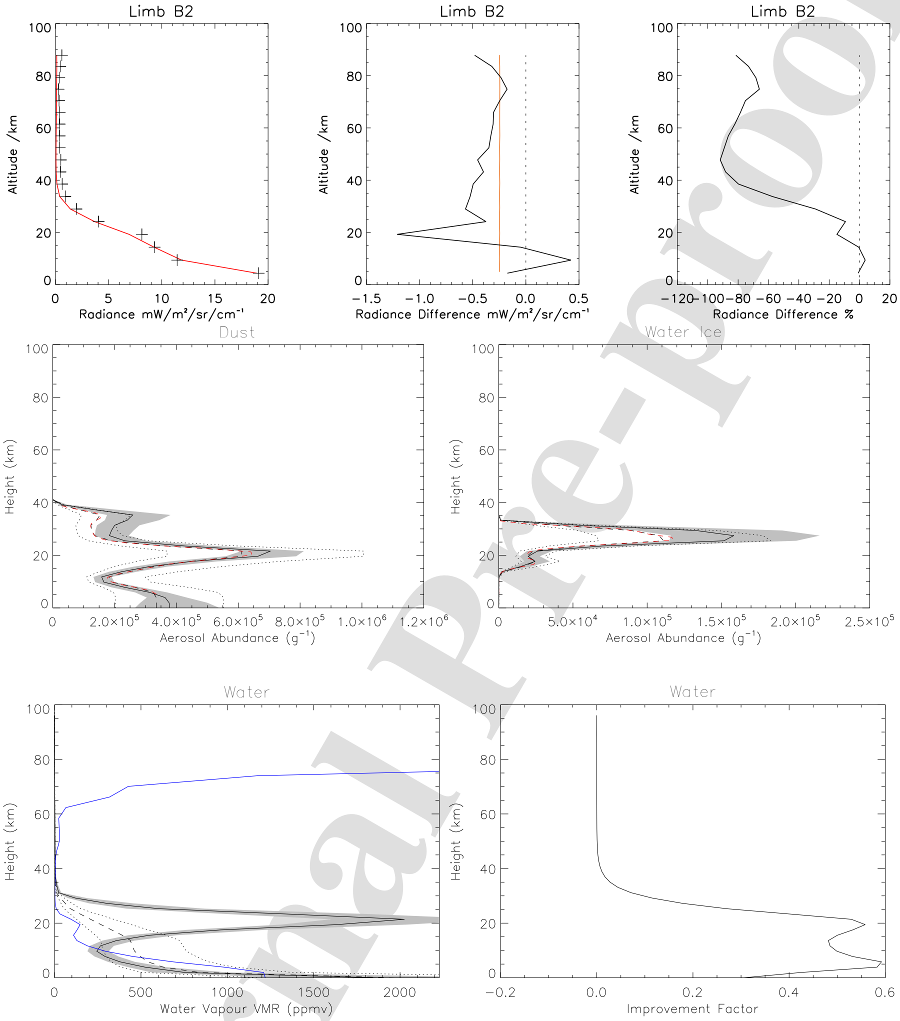

Figure 9: Example of Spurious Retrieval: **(Top Left)** Limb radiance fits where the red line corresponds to retrieval radiances and the black crosses indicate observed radiances, **(Top Middle)** difference between observed and retrieval radiances with radiance error including forward modelling error (orange line), **(Top Right)** percentage difference between observed and retrieval radiances, **(Middle Left)** dust abundance, **(Middle Right)** water ice abundance, **(Bottom Left)** retrieved water vapour profile and **(Bottom Right)** improvement factor. For plots, retrieved profile is black solid line with grey shaded error. The *a priori* profile and error are the dashed and dotted lines respectively and the blue line is the saturation VMR. Red lines are L2 profiles and errors. Observation is at L_s=114°, 86.583°N, 21.119°E at 1100 LST.

closer to the surface in the lower atmosphere above 5 km. Below 5 km, although retrieved profiles show water continuing to increase below this, the improvement factor (see Fig. 12) is decreasing rapidly and the retrieval will be relaxing back towards the *a priori*. The 'wetter' lower atmosphere can be identified in both the dayside and nightside results, with the vertical extension of the water vapour layer increasing in the NH. In the dayside, the expected results of a reasonably constant VMR down from the condensation level towards the ground (where again retrieval sensitivity trails off below 5 km) can be seen until high northern latitudes, where very high VMRs are present in the lower atmosphere at the seasonal caps. In the nightside results a similar pattern is seen, though the effects on the average profile of the high VMR DWL are more prevalent than on the dayside results.

In addition some inversion layers for water vapour close to the ground in the boundary layer can be seen northwards of the equator up to about 80°N. However, the reliability of the inversion layers result is debatable as they are in the region of decreasing sensitivity below about 5 km. Also, it is important to note that many of the L2 profiles used to create *a priori* profiles for the first stage retrievals were incomplete in their altitude coverage and had to be extrapolated for our retrievals (see the Section 5.1). This often means that where L2-based *a priori* profiles were used, the bottom 5–10 km of aerosol profiles in particular are part of that extrapolated range. These may be unreliable due to likely high limb path aerosol opacities seen this low in the atmosphere.

7. Discussion

7.1. Diurnal Variation in Vertical Water Vapour Profiles

Assessing diurnal variation is hampered by the poorer coverage for nightside results and high numbers of spurious profiles. Numerical calculations of the difference were made for bins where there is more than one profile for the equivalent dayside/nightside results of the same season. A selection of these results are given in Fig. 13 as these are representative of all the results. The difference was calculated as the difference between the average profiles of the bins in Figs. 10 & 11: $\mathrm{VMR}_{\mathrm{diff}} = \mathrm{VMR}_{\mathrm{night}} - \mathrm{VMR}_{\mathrm{day}}$. The error in the difference was calculated by adding the standard deviations of the day/night

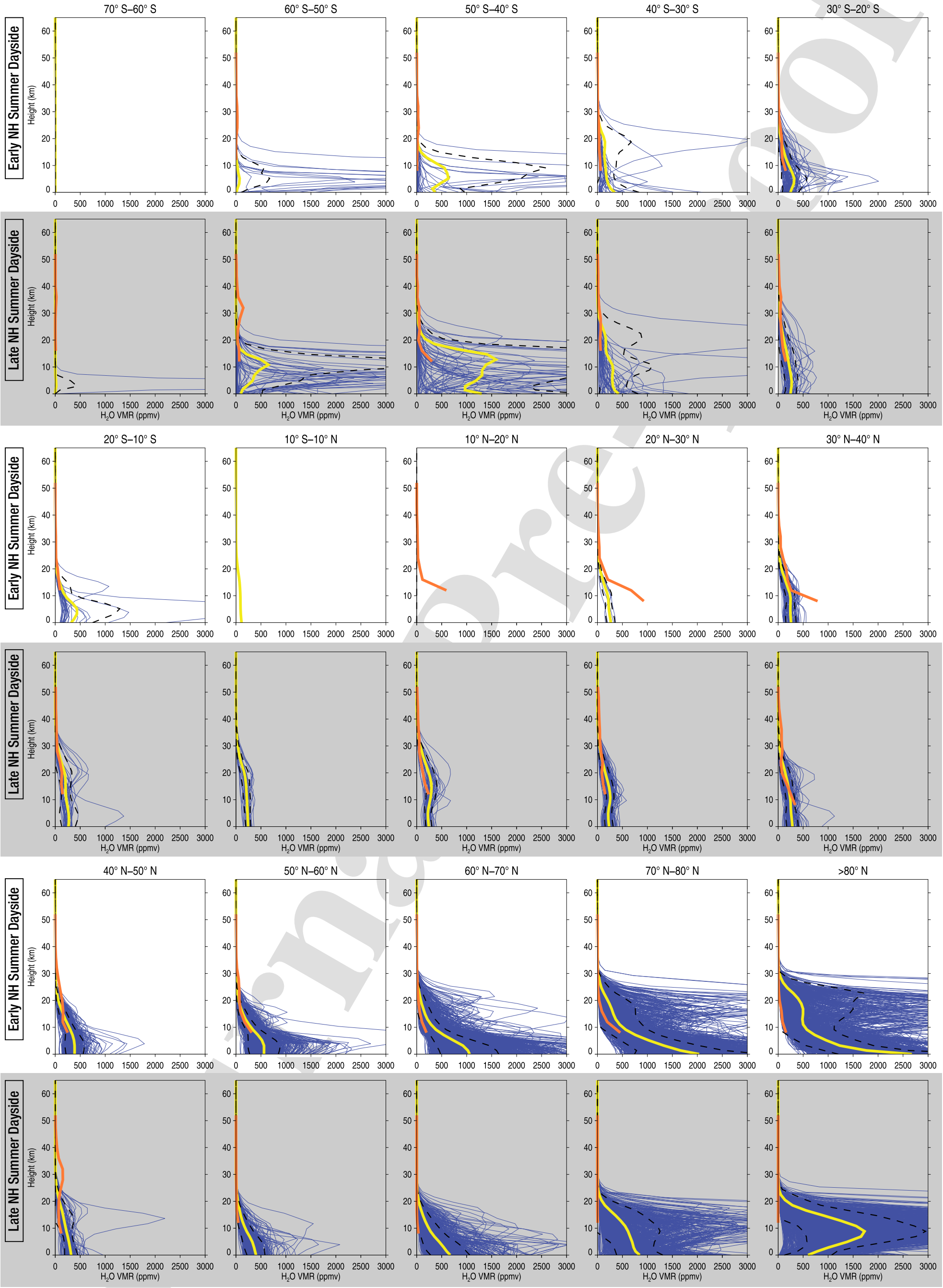

Figure 10: Dayside water retrievals with latitude bins for early/late NH summer on top of each other as marked. Profiles (blue lines) have been overplotted with mean (yellow line) and standard deviation (black dashed line). Profiles have been height shifted to the areoid and are overplotted with the CRISM results (orange line). Good agreement with CRISM results is seen.

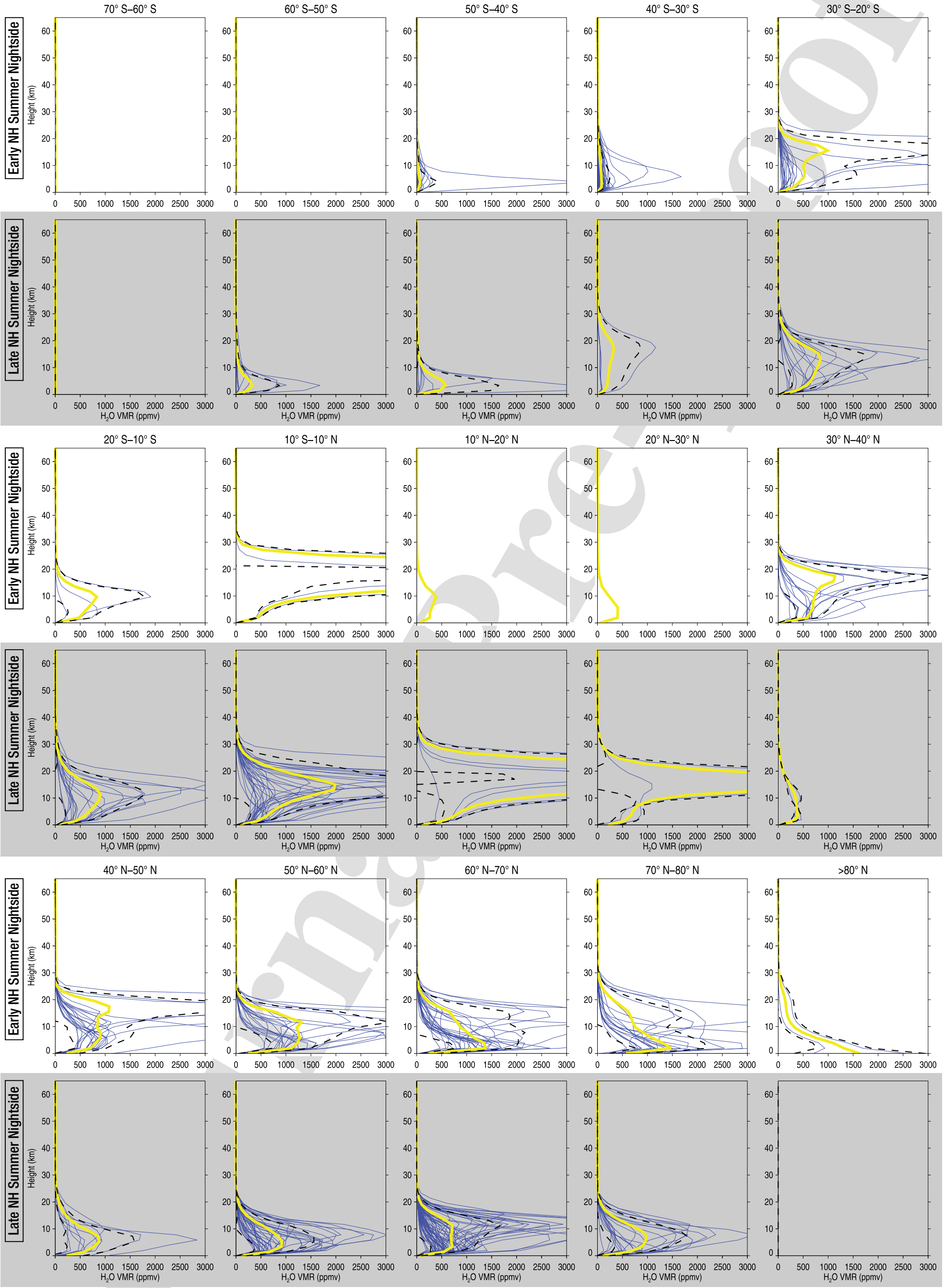

Figure 11: Nightside water retrievals with latitude bins for early/late NH summer on top of each other as marked. Profiles (blue lines) have been overplotted with mean (yellow line) and standard deviation (black dashed line).

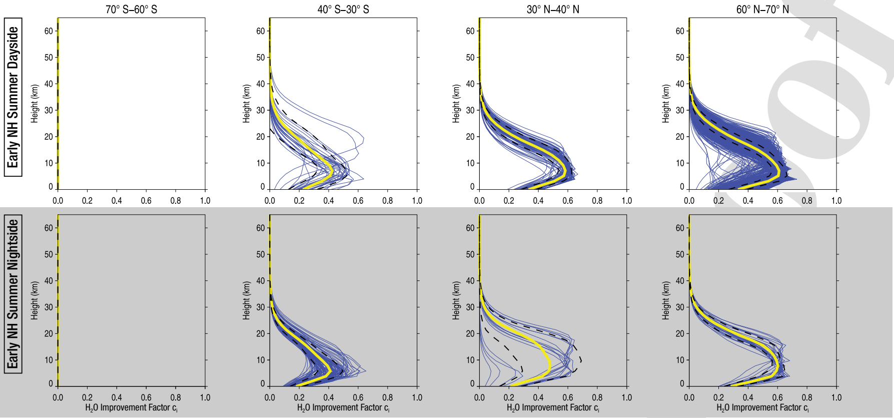

Figure 12: Improvement factor for Dayside/Nightside water retrievals for selected latitude bins for early NH summer on top of each other as marked. Profiles (blue lines) have been overplotted with mean (yellow line) and standard deviation (black dashed line). The improvment factor indicates information content in a retrieval, with values closer to one indicating more information.

average profiles in quadrature to calculate an RMS value. It can be clearly seen that the difference is almost exclusively smaller than the error except for a few cases near the surface. These differences are highly unlikely to be genuine as they are in the region where the retrieval is insensitive as it is relaxing back to the *a priori* (see Fig. 12).

There may be some genuine variation near the equator, with a decrease in the condensation height on the nightside, perhaps seen as condensation increasing the opacity of the aphelion cloud belt at night as discussed earlier (see Section 6.2). Unfortunately, this is difficult to disentangle from errors caused by high aerosol opacity. Overall, these results suggest that for heights above 5 km (those MCS is able to probe effectively) there is little significant diurnal variation in regions of low aerosol opacity. The greatest variation is likely to lie in these problematic high opacity areas (due to aerosol-water interaction) or much closer to the surface driven by surface interactions such as regolith exchange or sublimation from the seasonal cap.

7.2. Comparison of Vertical Water Profiles with CRISM Results

Using the results of Clancy et al. (2017) it is possible to perform validation of dayside retrievals, using their binned vertical profiles derived from CRISM retrievals of

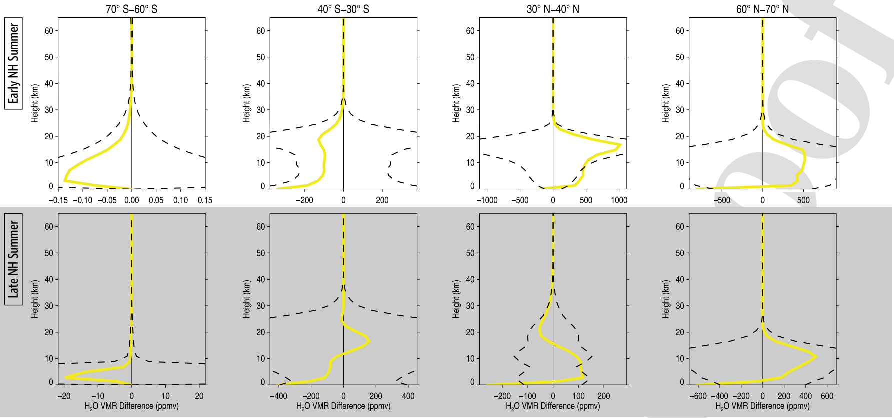

Figure 13: Diurnal variation for selected latitude bins. Difference (yellow line) is calculated as $VMR_{diff} = VMR_{night} - VMR_{day}$. Error (black dashed line) is the RMS of the standard deviations for the dayside and nightside profiles. Almost no diurnal variation can be seen outside of the error. For the regions where the difference is larger than error, near the surface, the retrieval is insensitive and relaxing back to the *a priori* (c.f. Fig. 12).

1.27 µm $O_2(^1\Delta_g)$ dayglow over ≥8–80 km altitudes. These comparisons are particularly appropriate as CRISM is also on MRO and so observations will have the same local surface times and similar observation geometries. Their observations range from 2009–2016 (MY29–33). Seasonal averages were obtained from two of their bins, L_s=100–140° and 140–200°, which can be compared with the early and late NH summer blocks respectively. Clancy et al. (2017) give uncertainties for the CRISM profiles as 20% (average uncertainties) below 20 km and 20–30% above (systematic uncertainties from modelling assumptions). The CRISM profiles have been drawn as orange lines on the dayside vertical profile plots in Fig. 10. To aid comparison water profiles in the figure have been mapped onto areoid heights rather than surface heights, the same as the CRISM data.

For the early NH summer dayside results, we see that at >80°N the CRISM profile fits within the profile envelope (i.e., the edges of the profiles group within a latitude bin) and 1σ. Moving southward an excellent match is seen between 80–50°N with the mean profile and the CRISM profile often being on top of one another. From 50–20°N our profiles and the CRISM data start to diverge, though still matching within the profiles envelope in 10–20 km range. Raised CRISM VMRs at 20–30 km are not seen in our results. And from 30°N towards the equator much larger abundances are seen below 10 km in CRISM data. Close matches are again seen in the 10–40°S band and then within the envelope for the remaining SH profiles. At 40–60°S, we see matching within the envelope, with some water layers at 35 km in CRISM profiles, but not ours.

For late NH summer results we see close matches at altitudes >20 km in the >80–70°N range with matching within the profile envelope below this. Close matching is seen in the 70–10°N region below 30 km. Above 30 km in the 50–30°N region some layers of higher abundance are seen in the CRISM profiles, but not ours. In the SH close matches are seen from 10–30°S. A good match is again seen polewards of this for the regions where CRISM data are available.

Overall excellent agreement is found between our vertical retrievals and the CRISM dataset, particularly in the 80–50°N latitude band, where the water abundances are highest. Disagreements between the datasets come in three types: a) layers of water at ≥30 km which appear in the CRISM data but not ours b) regions where our retrievals have higher or lower abundances and match only within the profiles envelope and c) regions in the tropics where our retrievals have significantly lower abundances below 15 km.

These differences may be caused by a lack of sensitivity in our retrieval at higher altitudes or interannual variation as CRISM data are from MY29–33 and ours are from MY28. Lack of high altitude sensitivity is supported by Fig. 12, where at altitudes ≥30 km the improvement factor is near zero. Regions where profiles only match within the profile envelope or in the tropics correspond to regions of high aerosol abundance and hence areas where spurious retrievals are more probable. Interestingly, when Clancy et al. (2017) compared CRISM results with SPICAM solar occultation water vapour profiles, a similar result to c) was seen, with lower abundances in the SPICAM results below 30 km, though this was for L_s=80–105 at 40–60°N. It was posited that difference was due to possible variability in cloud conditions caused by differences in local time, as solar occultation profiles follow the terminator and CRISM results are at 15h. Given that MCS and CRISM results are at the same local time, this explanation would not apply to our results. On the whole, despite these differences, the results of

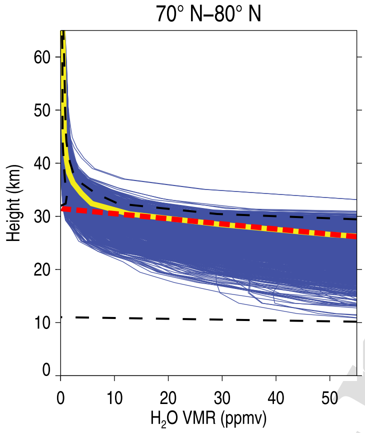

Figure 14: Figure showing example extrapolation (red dashed line) used to calculate profile top for the 70–80°N bin of the early NH summer dayside retrievals. Profiles (blue lines) have been overplotted with mean (yellow line) and standard deviation (black dashed line).

our comparison with the CRISM profiles are very encouraging.

7.3. Seasonal Variation of Vertical Water Profiles

Evidence of seasonal variation is seen in the dayside results, in the form of variation of the zonally averaged hygropause (vertical extent) which acts as an approximation to the zonally averaged condensation level of the water profiles. The early NH summer results have higher hygropause levels at mid to high latitudes and these are greater also than the equivalent latitude range in the late NH summer. The hygropause levels in early NH summer results then decrease towards the south pole. During the late NH summer we see the highest hygropause levels in the equatorial regions and the tropics (mean profile reaching >30 km) with lower levels in northern mid to high latitudes. Late NH summer hygropause levels are higher than their early NH summer equivalents in the southern tropics, equator and northern tropics. This matches the variation of zonally averaged condensation levels from TES results seen in Smith (2002). Similar behaviour is seen in the CRISM results. The nightside results are somewhat noisier but the same pattern seems to be present.

To visualise this behaviour more easily, we created a quantity dubbed the 'profile top', to use as a proxy for the hygropause and hence an approximation for the condensation level. This is calculated by manually extrapolating the top ‘flat’ part of the average water profile from a latitude bin, to the axis, as demonstrated in Fig. 14. An error of ±2.5 km was estimated for the profile top due to the extrapolation. The profile top versus latitude was then overplotted on the ice opacity retrievals in Fig. 5. Due to the process of extrapolation and the fact that the hygropause may not exactly track the condensation level, there is likely to be a positive systematic offset between the profile top and the real condensation level, i.e., it is higher than the condensation level, but it should still track direction of change (i.e., an increase or decrease). An additional source of error comes from the water profiles themselves, as the profile top extrapolation uses the average profile which in turn will include some spurious high DWL results. Despite these caveats the behaviour discussed above is also seen on these plots. The profile top is higher in the equator and tropics during the late summer, along with an aphelion belt that is higher and weaker. This verifies its reliability as a first-order approximation of the condensation level.

These seasonal difference results show the variation in vertical behaviour as water vapour is transported by the Hadley circulation. In the early NH summer water is transported southward in the cross-equatorial Hadley cell, while during the course of the late NH summer the Hadley circulation splits into its equinoctial two-cell configuration. The potential link between the aphelion cloud belt and changes in the water vapour condensation level was suggested by Clancy et al. (1996) and further discussed in Smith (2002). In our results the variation in condensation level is tracked by the variation in the aphelion cloud belt strength and vertical extent (see Fig. 5). When the level is high, water reaches higher levels before condensing. The higher levels at the equator and tropics in late NH summer then make the aphelion cloud belt weaker in late NH summer than early NH summer. A schematic diagram showing this process is given in Fig. 15.

8. Conclusions

Retrievals of water vapour were performed using observations from MCS during MY28 L_s=111–173° (NH summer) and split into early (111–140°) and late NH

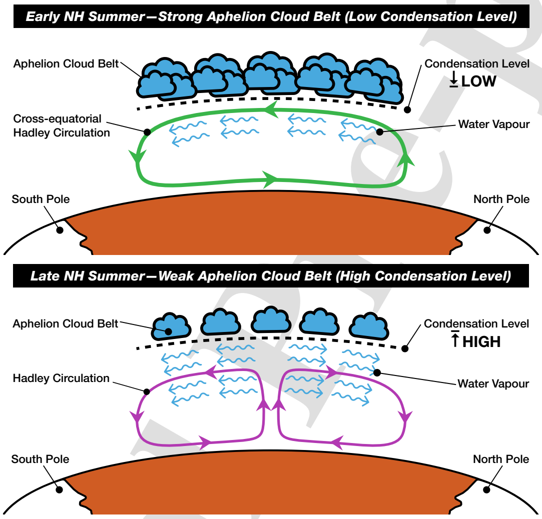

Figure 15: Simplified schematic showing how seasonal variation of condensation level changes the strength of the Aphelion Belt. During early NH summer the condensation level is lower at the equator and tropics resulting in more water vapour condensing and a stronger cloud belt. In late NH summer the condensation level has risen in the tropics and equator, reducing the amount of water vapour condensing resulting in a weaker cloud belt.

summer (140–173°) blocks. Despite difficulties and a limited number of nightside retrievals, there has been success in reproducing expected seasonal trends alongside some unexpected results. Discounting the contribution from spurious supersaturated DWL, column abundances match the expected pattern with greater abundances in the summer NH at the edge of the polar cap gradually decreasing southwards.

Seasonal variation in the vertical extent of water vapour has been observed following the seasonal changes in condensation level. This also shows the vertical aspect of behaviour, as water vapour is transported southward in the cross-equatorial Hadley cell in early NH summer, while during the course of the late NH summer the Hadley circulation splits into its equinoctial two-cell configuration. In conjunction with our ice retrievals this has allowed direct observation of vertical interaction/evolution between the transported water vapour and the aphelion cloud belt for the first time. Seasonal changes in the vertical extent are seen to have an impact on the cloud belt. When the condensation level is high water reaches higher levels before condensing. The higher levels at the equator and tropics in late NH summer then make the aphelion cloud belt weaker in late NH summer than early NH summer. This was supported by our use of the profile top metric as an approximation for the zonally averaged condensation level in Fig. 5.

Nightside vertical profiles of water vapour have been retrieved for the first time. Unfortunately, due to higher ice opacities at night, retrievals are noisier and the coverage is not as extensive as for the dayside. Having both dayside and nightside retrievals allows direct comparison for diurnal variation. No significant diurnal variation above error was observed in regions of lower aerosol opacity. Comparison in regions of higher aerosol opacity are frustrated by retrieval inaccuracy and poor coverage. Unfortunately, these regions are one of the most likely types to see variation due to aerosol-water interaction (e.g., cloud formation). Another potential region is at near-surface altitudes where surface interaction may be observed (e.g., adsorption). Here, MCS's extended detector FOV-wings along with higher opacities hamper effective retrievals.

A number of unphysical supersaturated DWL observations have been noted in our results and future work will require their identification and removal. The cause seems to be the false attribution by the retrieval of B2 radiances from aerosol as water for high dust and ice limb path opacities and is supported by results from retrieval sensitivity simulations. Such profiles could potentially be identified through the use of a limb opacity per kilometre threshold in A5 for dust and A4 for ice, as high aerosol abundances are likely to produce unreliable water results.

Consistency with historical datasets for water vapour column abundance (TES, SPICAM and ground-based) was seen. For vertical profiles good agreement was found in comparisons with the CRISM vertical profile data of Clancy et al. (2017). Some disagreement was found at higher altitudes in the form of detached water layers and lower abundances above about 30 km. The lower abundances above 30 km suggested that our retrievals suffer reduced sensitivity at higher altitudes. This was supported by our improvement factor profiles in Fig. 12.

The radiometric errors induced by choice of aerosol size distribution have led to retrievals that require higher forward modelling errors. This provides lower radiance constraint for the retrieval and has likely led to the reduced sensitivity of our water retrievals at higher altitudes where radiances are low. To resolve this in the future it would be best to develop a retrieval methodology where the aerosol extinction cross-section was also retrieved using an aerosol-sensitive far infrared channel such as B1 (which is still transparent in regions where the mid-infrared channels A4 and A5 would be opaque). As B1 (31.7 µm) is much closer in wavelength to B2 (41.7 µm) than A4 (11.8 µm) or A5 (22.2 µm) this could then be used to extrapolate to the extinction cross-section at B2. This should eliminate spurious radiance contributions in B2 from aerosols and would allow tighter radiance constraints (lower forward modelling errors) increasing high altitude sensitivity. In conjunction with a first stage retrieval using a far infrared channel such as B1, it would also allow the retrieval of water to lower altitudes in regions of higher limb opacity than previously possible. This could potentially allow examination of the boundary layer and surface interaction. Some early work on extinction cross-section retrieval for MCS has been done by Kleinböhl et al. (2017, 2018).

On a related note, if aerosol particles are significantly larger than assumed in this work, then there is a corresponding increase in single-scattering albedo, meaning that the radiance contribution from scattering at B2 may no longer negligible and would need to be included in the forward model.

Overall, it can be concluded that retrievals from MCS have provided some new limits on diurnal variation and insight into the current state of the Martian water cycle in its interaction with the aphelion cloud belt. However, without the additional retrieval of aerosol extinction cross-section it is unlikely that the full potential of MCS's abilities for vertical water profile retrievals will be realised.

9. Acknowledgements

This research was funded by the UK Science and Technology Facilities Council and the UK Space Agency and the NASA/GSFC Internal Scientist Funding Model (ISFM) Exospheres, Ionospheres, Magnetospheres Modeling (EIMM) team. The work done through the Center for Research and Exploration in Space Science and Technology (CRESST-II) is supported by NASA award number 80GSFC21M0002. The authors would like to thank M. Smith for kindly providing TES data used in this study and for the helpful insight given by the reviewers. The authors would also like to thank the MRO spacecraft and MCS instrument operations teams who made these measurements possible. In particular, A. Kleinböhl and D.M. Kass of NASA/JPL for many helpful comments, clarifications and expertise on MRO/MCS.

References

Baker, V.R., Strom, R.G., Gulick, V.C., Kargel, J.S., Komatsu, G., 1991. Ancient oceans, ice sheets and the hydrological cycle on Mars. Nature 352, 589–594. doi:10.1038/352589a0.

Boynton, W.V., Feldman, W.C., Squyres, S.W., Prettyman, T.H., Brückner, J., Evans, L.G., Reedy, R.C., Starr, R., Arnold, J.R., Drake, D.M., Englert, P.A.J., Metzger, A.E., Mitrofanov, I., Trombka, J.I., d'Uston, C., Wänke, H., Gasnault, O., Hamara, D.K., Janes, D.M., Marcialis, R.L., Maurice, S., Mikheeva, I., Taylor, G.J., Tokar, R., Shinohara, C., 2002. Distribution of Hydrogen in the Near Surface of Mars: Evidence for Subsurface Ice Deposits. Science 297, 81–85. doi:10.1126/science.1073722.

Chahine, M.T., 1970. Inverse Problems in Radiative Transfer: Determination of Atmospheric Parameters. Journal of Atmospheric Sciences 27, 960–967. doi:10.1175/1520-0469(1970)027<0960:IPIRTD>2.0.CO;2.

Chahine, M.T., 1972. A General Relaxation Method for Inverse Solution of the Full Radiative Transfer Equation. Journal of Atmospheric Sciences 29, 741–747. doi:10.1175/1520-0469(1972)029<0741:AGRMFI>2.0.CO;2.

Clancy, R.T., Grossman, A.W., Wolff, M.J., James, P.B., Rudy, D.J., Billawala, Y.N., Sandor, B.J., Lee, S.W., Muhleman, D.O., 1996. Water vapor saturation at low altitudes around Mars aphelion: A key to Mars climate? Icarus 122, 36–62. doi:10.1006/icar.1996.0108.

Clancy, R.T., Sandor, B.J., Wolff, M.J., Christensen, P.R., Smith, M.D., Pearl, J.C., Conrath, B.J., Wilson, R.J., 2000. An intercomparison of ground-based millimeter, MGS TES, and Viking atmospheric temperature measurements: Seasonal and interannual variability of temperatures and dust loading in the global Mars atmosphere. Journal of Geophysical Research 105, 9553–9572. doi:10.1029/1999JE001089.

Clancy, R.T., Smith, M.D., Lefèvre, F., McConnochie, T.H., Sandor, B.J., Wolff, M.J., Lee, S.W., Murchie, S.L., Toigo, A.D., Nair, H., Navarro, T., 2017. Vertical profiles of Mars 1.27 μm O_2 dayglow from MRO CRISM limb spectra: Seasonal/global behaviors, comparisons to LMDGCM simulations, and a global definition for Mars water vapor profiles. Icarus 293, 132–156. doi:10.1016/j.icarus.2017.04.011.

Conrath, B.J., 1975. Thermal structure of the Martian atmosphere during the dissipation of the dust storm of 1971. Icarus 24, 36–46.

Fedorova, A., Bertaux, J.L., Betsis, D., Montmessin, F., Korablev, O., Maltagliati, L., Clarke, J., 2018. Water vapor in the middle atmosphere of Mars during the 2007 global dust storm. Icarus 300, 440–457. doi:10.1016/j.icarus.2017.09.025.

Fedorova, A.A., Korablev, O.I., Bertaux, J.L., Rodin, A.V., Montmessin, F., Belyaev, D.A., Reberac, A., 2009. Solar infrared occultation observations by SPICAM experiment on Mars-Express: Simultaneous measurements of the vertical distributions of H_2O, CO_2 and aerosol. Icarus 200, 96–117. doi:10.1016/j.icarus.2008.11.006.

Forget, F., Dassas, K., Wanherdrick, Y., Lewis, S.R., Collins, S.J., Bingham, S.J., 2005. Mars Climate Database v4.1 User Manual.

Forget, F., Millour, E., Lebonnois, S., Montabone, L., Dassas, K., Lewis, S.R., Read, P.L., López-Valverde, M.A., González-Galindo, F., Montmessin, F., Lefèvre, F., Desjean, M.C., Huot, J.P., 2006. The new Mars climate database, in: Forget, F., Lopez-Valverde, M.A., Desjean, M.C., Huot, J.P., Lefevre, F., Lebonnois, S., Lewis, S.R., Millour, E., Read, P.L., Wilson, R.J. (Eds.), Mars Atmosphere Modelling and Observations, pp. 128–+.

Hansen, G.B., 2003. Infrared Optical Constants of Martian Dust Derived from Martian Spectra [CD-ROM], in: Albee, A.L., Kieffer, H.H. (Eds.), Sixth International Conference on Mars, p. 3194.

Hansen, J.E., Travis, L.D., 1974. Light scattering in planetary atmospheres. Space Science Reviews 16, 527–610.

Hurley, J., Teanby, N.A., Irwin, P.G.J., Calcutt, S.B., Sefton-Nash, E., 2014. Differentiability and retrievability of CO_2 and H_2O clouds on Mars from MRO/MCS measurements: A radiative-transfer study. Planetary and Space Science 97, 65–84. doi:10.1016/j.pss.2014.03.015.

Irwin, P.G.J., 2009. Giant Planets of Our Solar System: Atmospheres, Composition, and Structure, 2nd ed. Springer Praxis Books, Volume ISBN 978-3-540-85157-8. Springer Berlin Heidelberg, 2009. doi:10.1007/978-3-540-85158-5.

Irwin, P.G.J., Teanby, N.A., de Kok, R., Fletcher, L.N., Howett, C.J.A., Tsang, C.C.C., Wilson, C.F., Calcutt, S.B., Nixon, C.A., Parrish, P.D., 2008. The NEMESIS planetary atmosphere radiative transfer and retrieval tool. Journal of Quantitative Spectroscopy and Radiative Transfer 109, 1136–1150. doi:10.1016/j.jqsrt.2007.11.006.

Kleinböhl, A., Chen, L., Schofield, J.T., 2017. Far Infrared Spectroscopic Parameters of Mars Atmospheric Aerosols and their Application to MCS Retrievals in High

Aerosol Conditions, in: Forget, F., Millour, M. (Eds.), The Mars Atmosphere: Modelling and observation, p. 2230.

Kleinböhl, A., Schofield, J., Kass, D., 2018. Water ice cloud profiles during the aphelion season on Mars retrieved from Mars Climate Sounder far-infrared radiance measurements, in: 42nd COSPAR Scientific Assembly, pp. B4.1–32–18.

Kleinböhl, A., Schofield, J.T., Abdou, W.A., Irwin, P.G.J., de Kok, R.J., 2011. A single-scattering approximation for infrared radiative transfer in limb geometry in the Martian atmosphere. Journal of Quantitative Spectroscopy and Radiative Transfer 112, 1568–1580. doi:10.1016/j.jqsrt.2011.03.006.

Kleinböhl, A., Schofield, J.T., Kass, D.M., Abdou, W.A., Backus, C.R., Sen, B., Shirley, J.H., Lawson, W.G., Richardson, M.I., Taylor, F.W., Teanby, N.A., McCleese, D.J., 2009. Mars Climate Sounder limb profile retrieval of atmospheric temperature, pressure, and dust and water ice opacity. Journal of Geophysical Research (Planets) 114, 10006–+. doi:10.1029/2009JE003358.

Krasnopolsky, V.A., 2015. Variations of the HDO/H_2O ratio in the martian atmosphere and loss of water from Mars. Icarus 257, 377–386. doi:10.1016/j.icarus.2015.05.021.

Krasnopolsky, V.A., Korablev, O.I., Moroz, V.I., Krysko, A.A., Blamont, J.E., Chassefiere, E., 1991. Infrared solar occultation sounding of the Martian atmosphere by the Phobos spacecraft. Icarus 94, 32–44. doi:10.1016/0019-1035(91)90139-K.

Lacis, A.A., Oinas, V., 1991. A description of the correlated-k distribution method for modelling nongray gaseous absorption, thermal emission, and multiple scattering in vertically inhomogeneous atmospheres. Journal of Geophysical Research 96, 9027–9064.

Lolachi, R., 2019. Hunting for Water with MCS: Assessing the Retrievability of Water Vapour with Mars Climate Sounder. Ph.D. thesis. University of Oxford. Atmospheric, Oceanic & Planetary Physics, Department of Physics, University of Oxford, Clarendon Laboratory, Parks Road, Oxford, OX1 3PU, UK. https://ora.ox.ac.uk/objects/uuid:300fd088-f809-45bd-82a3-5c27e0093d43.

Maltagliati, L., Montmessin, F., Fedorova, A., Korablev, O., Forget, F., Bertaux, J.L., 2011a. Evidence of Water Vapor in Excess of Saturation in the Atmosphere of Mars. Science 333, 1868–1871. doi:10.1126/science.1207957.

Maltagliati, L., Montmessin, F., Korablev, O., Fedorova, A., Forget, F., Määttänen, A., Lefèvre, F., Bertaux, J.L., 2013. Annual survey of water vapor vertical distribution and water-aerosol coupling in the martian atmosphere observed by SPICAM/MEx solar occultations. Icarus 223, 942–962. doi:10.1016/j.icarus.2012.12.012.

Maltagliati, L., Titov, D.V., Encrenaz, T., Melchiorri, R., Forget, F., Keller, H.U., Bibring, J.P., 2011b. Annual survey of water vapor behavior from the OMEGA mapping spectrometer onboard Mars Express. Icarus 213, 480–495. doi:10.1016/j.icarus.2011.03.030.

McCleese, D.J., Heavens, N.G., Schofield, J.T., Abdou, W.A., Bandfield, J.L., Calcutt, S.B., Irwin, P.G.J., Kass, D.M., Kleinböhl, A., Lewis, S.R., Paige, D.A., Read, P.L., Richardson, M.I., Shirley, J.H., Taylor, F.W., Teanby, N., Zurek, R.W., 2010. Structure and dynamics of the Martian lower and middle atmosphere as observed by the Mars Climate Sounder: Seasonal variations in zonal mean temperature, dust, and water ice aerosols. Journal of Geophysical Research (Planets) 115, 12016. doi:10.1029/2010JE003677.

McCleese, D.J., Schofield, J.T., Taylor, F.W., Calcutt, S.B., Foote, M.C., Kass, D.M., Leovy, C.B., Paige, D.A., Read, P.L., Zurek, R.W., 2007. Mars Climate Sounder: An investigation of thermal and water vapor structure, dust and condensate distributions in the atmosphere, and energy balance of the polar regions. Journal of Geophysical Research (Planets) 112, E05S06. doi:10.1029/2006JE002790.

Melchiorri, R., Encrenaz, T., Fouchet, T., Drossart, P., Lellouch, E., Gondet, B., Bibring, J.P., Langevin, Y., Schmitt, B., Titov, D., Ignatiev, N., 2007. Water vapor mapping on Mars using OMEGA/Mars Express. Planetary and Space Science 55, 333–342. doi:10.1016/j.pss.2006.05.040.

Montmessin, F., Korablev, O., Lefèvre, F., Bertaux, J.L., Fedorova, A., Trokhimovskiy, A., Chaufray, J.Y., Lacombe, G., Reberac, A., Maltagliati, L., Willame, Y., Guslyakova, S., Gérard, J.C., Stiepen, A., Fussen, D., Mateshvili, N., Määttänen, A., Forget, F., Witasse, O., Leblanc, F., Vandaele, A.C., Marcq, E., Sandel, B., Gondet, B., Schneider, N., Chaffin, M., Chapron, N., 2017a. SPICAM on Mars Express: A 10 year in-depth survey of the Martian atmosphere. Icarus 297, 195–216. doi:10.1016/j.icarus.2017.06.022.

Montmessin, F., Smith, M.D., Langevin, Y., Mellon, M.T., Fedorova, A., 2017b. The Water Cycle, in: Haberle, R.M., Clancy, R.T., Forget, F., Smith, M.D., Zurek, R.W. (Eds.), The atmosphere and climate of Mars. Cambridge University Press, Cambridge, pp. 338–373. doi:10.1017/9781139060172.011.

Pankine, A.A., Tamppari, L.K., Smith, M.D., 2009. Water vapor variability in the north polar region of Mars from Viking MAWD and MGS TES datasets. Icarus 204, 87–102. doi:10.1016/j.icarus.2009.06.009.

Puliafito, E., Bevilacqua, R., Olivero, J., Degenhardt, W., 1995. Retrieval error comparison for several inversion techniques used in limb-scanning millimeter-wave spectroscopy. Journal of Geophysical Research 100, 14,257–14,267. doi:10.1029/95JD00212.

Read, P., Lewis, S., 2004. The Martian Climate Revisited: Atmosphere and Environment of a Desert Planet. UK: Springer-Praxis.

Rodgers, C.D., 2000. Inverse Methods for Atmospheric Sounding: Theory and Practice; Series on Atmospheric, Oceanic and Planetary Physics Vol. 2. World Scientific.

Rodin, A.V., Korablev, O.I., Moroz, V.I., 1997. Vertical Distribution of Water in the Near-Equatorial Troposphere of Mars: Water Vapor and Clouds. Icarus 125, 212–229. doi:10.1006/icar.1996.5602.

Rothman, L.S., Jacquemart, D., Barbe, A., Chris Benner, D., Birk, M., Brown, L.R., Carleer, M.R., Chackerian, C., Chance, K., Coudert, L.H., Dana, V., Devi, V.M., Flaud, J.M., Gamache, R.R., Goldman, A., Hartmann, J.M., Jucks, K.W., Maki, A.G., Mandin, J.Y., Massie, S.T., Orphal, J., Perrin, A., Rinsland , C.P., Smith, M.A.H., Tennyson, J., Tolchenov, R.N., Toth, R.A., Vander Auwera, J., Varanasi, P., Wagner, G., 2005. The HITRAN 2004 molecular spectroscopic database. Journal of Quantitative Spectroscopy and Radiative Transfer 96, 139–204. doi:10.1016/j.jqsrt.2004.10.008.

Sefton-Nash, E., Teanby, N.A., Montabone, L., Irwin, P.G.J., Hurley, J., Calcutt, S.B., 2013. Climatology and first-order composition estimates of mesospheric clouds from Mars Climate Sounder limb spectra. Icarus 222, 342–356. doi:10.1016/j.icarus.2012.11.012.

Smith, M.D., 2002. The annual cycle of water vapor on Mars as observed by the Thermal Emission Spectrometer. Journal of Geophysical Research (Planets) 107, 25–1. doi:10.1029/2001JE001522.

Smith, M.D., 2008. Spacecraft Observations of the Martian Atmosphere. Annual Review of Earth and Planetary Sciences 36, 191–219. doi:10.1146/annurev.earth.36.031207.124334.

Spinrad, H., Münch, G., Kaplan, L.D., 1963. Letter to the Editor: the Detection of Water Vapor on Mars. Astrophysical Journal 137, 1319–+. doi:10.1086/147613.

Trokhimovskiy, A., Fedorova, A., Korablev, O., Montmessin, F., Bertaux, J.L., Rodin, A., Smith, M.D., 2015. Mars' water vapor mapping by the SPICAM IR spectrometer: Five martian years of observations. Icarus 251, 50–64. doi:10.1016/j.icarus.2014.10.007.

Vandaele, A.C., Korablev, O., Daerden, F., Aoki, S., Thomas, I.R., Altieri, F., López-Valverde, M., Villanueva, G., Liuzzi, G., Smith, M.D., Erwin, J.T., Trompet, L., Fedorova, A.A., Montmessin, F., Trokhimovskiy, A., Belyaev, D.A., Ignatiev, N.I., Luginin, M., Olsen, K.S., Baggio, L., Alday, J., Bertaux, J.L., Betsis, D., Bolsée, D., Clancy, R.T., Cloutis, E., Depiesse, C., Funke, B., Garcia-Comas, M., Gérard, J.C., Giuranna, M., Gonzalez-Galindo, F., Grigoriev, A.V., Ivanov, Y.S., Kaminski, J., Karatekin, O., Lefèvre, F., Lewis, S., López-Puertas, M., Mahieux, A., Maslov, I., Mason, J., Mumma, M.J., Neary, L., Neefs, E., Patrakeev, A., Patsaev, D., Ristic, B., Robert, S., Schmidt, F., Shakun, A., Teanby, N.A., Viscardy, S., Willame, Y., Whiteway, J., Wilquet, V., Wolff, M.J., Bellucci, G., Patel, M.R., López-Moreno, J.J., Forget, F., Wilson, C.F., Young, R., Svedhem, H., Vago, J.L., Rodionov, D., NOMAD Science Team, ACS Science Team, 2019. Martian dust storm impact on atmospheric H_2O and D/H observed by ExoMars Trace Gas Orbiter. Nature 568, 521–525. doi:10.1038/s41586-019-1097-3.

Warren, S.G., 1984. Optical constants of ice from the ultraviolet to the microwave. Applied Optics 23, 1206–1225.

Warren, S.G., Brandt, R.E., 2008. Optical constants of ice from the ultraviolet to the microwave: A revised compilation. Journal of Geophysical Research (Atmospheres) 113, 14220. doi:10.1029/2007JD009744.

Wolff, M.J., Clancy, R.T., 2003. Constraints on the size of Martian aerosols from Thermal Emission Spectrometer observations. Journal of Geophysical Research (Planets) 108, 1–1. doi:10.1029/2003JE002057.

Wolff, M.J., Smith, M.D., Clancy, R.T., Spanovich, N., Whitney, B.A., Lemmon, M.T., Bandfield, J.L., Banfield, D., Ghosh, A., Landis, G., Christensen, P.R., Bell, J.F., Squyres, S.W., 2006. Constraints on dust aerosols from the Mars Exploration Rovers using MGS overflights and Mini-TES. Journal of Geophysical Research (Planets) 111, 12–+. doi:10.1029/2006JE002786.

Highlights

3 to 5 bullet points (maximum 85 characters, including spaces, per bullet point).

- MCS used to retrieve vertical water profiles for first time (NH summer, MY28).
- Column abundances and vertical profiles match well to results from others.
- Interaction between aphelion cloud belt and water vapour condensation level seen.

Declaration of interests

☒ The authors declare that they have no known competing financial interests or personal relationships that could have appeared to influence the work reported in this paper.

☐The authors declare the following financial interests/personal relationships which may be considered as potential competing interests: